

Investigating pulsating variables and eclipsing binaries in NGC 2126 using ground- and space-based photometry, astrometry, spectroscopy, and modelling

Athul Dileep^{1,2★}, Santosh Joshi¹, Sneha Lata,¹ Patricia Lampens,³ Peter De Cat³,
 Sebastian Zúñiga-Fernández⁴, David Mkrtychian⁵, Pramod Kumar S.,⁶ Mrinmoy Sarkar,^{1,2}
 Alaxender Panchal,^{1,7} Yogesh C. Joshi¹, Rishi C.,¹ Neelam Panwar,¹ Arjav Jain¹ and Neeraj Rathore⁸

¹Aryabhata Research Institute of Observational Sciences (ARIES), Manora Peak, Nainital 263002, Uttarakhand, India

²Department of Applied Physics, M.J.P. Rohilkhand University, Bareilly 243006, Uttar Pradesh, India

³Royal Observatory of Belgium (ROB), Av. Circulaire 3, B-1180 Uccle, Belgium

⁴Astrobiology Research Unit, Université de Liège, Allée du 6 Août 19C, B-4000 Liège, Belgium

⁵National Astronomical Research Institute of Thailand (NARIT), Chiang Mai 50180, Thailand

⁶Indian Institute of Astrophysics (IIA), Bangalore 560034, Karnataka, India

⁷Physical Research Laboratory (PRL), Ahmedabad 380009, Gujarat, India

⁸Department of Physics, Bareilly College, Bareilly 243005, Uttar Pradesh, India

Accepted 2025 February 24. Received 2025 February 24; in original form 2024 October 31

ABSTRACT

Pulsating variables are prevalent in the classical δ Scuti instability strip of intermediate-age open star clusters. The cluster membership of these stars facilitates a comparative analysis of their evolution in analogous environments. In this study, we integrate ground-based observations, *Transiting Exoplanet Survey Satellite* (*TESS*) Full Frame Images (FFIs), and *Gaia* Data Release 3 (DR3) data to investigate variable stars in the intermediate-age open star cluster NGC 2126. We performed ground-based time-series observations of NGC 2126 to identify variable stars within its vicinity. Next, we determined the membership of these stars using parallax and the proper motions from *Gaia* DR3 archive. Then, we searched the *TESS* FFIs for counterparts to the variables identified above and performed their frequency analysis and classification. Finally, we modelled the light curves (LCs) of detected eclipsing binaries (EBs), including V551 Aur, which has a pulsating component. We found 25 members and 85 field variable stars. In *TESS* FFIs, we found LCs for 11 known variables and a new rotational variable. We determined that the pulsating EB V551 Aur is a member of the cluster. The low- and medium-resolution spectra revealed the line profile variation and the basic parameters for the star, respectively. Simultaneous modelling of the eclipses and the embedded pulsations resulted in improved orbital parameters for the binary system. We also report the determination of orbital parameters for the previously uncharacterized EB system UCAC4 700–043174.

Key words: techniques: photometric – binaries: eclipsing – stars: oscillations – stars: variables: general – open clusters and associations: individual: NGC 2126 – techniques: spectroscopic .

1 INTRODUCTION

Open star clusters comprise stars that have emerged from a common molecular cloud and are gravitationally bound to one another. Consequently, they possess analogous ages, distances, and initial chemical compositions. The membership of stars within an open cluster imposes constraints, especially regarding their age in comparison to the ambiguously determined ages of field stars. Thus, examining stars that are constituents of an open cluster is more advantageous than analysing field stars. Diverse independent methodologies for stellar characterization, such as asteroseismology (Aerts 2021), can gain from open clusters by imposing supplementary constraints on parameters such as age and mass (Bedding et al. 2023; Pamos Ortega

et al. 2023; Li et al. 2024). The intermediate-age open star clusters possess their turn-off point adjacent to the classical instability strip, thereby hosting a variety of pulsating variable stars of spectral type A and F, including δ Scuti stars and γ Doradus stars (Chehlaeh et al. 2018).

Ground-based studies of open clusters yield ensemble photometry for a collection of stars within a defined area. The Aryabhata Research Institute of Observational Sciences (ARIES) in Nainital, India, possesses photometric observational facilities in the Northern hemisphere, which are very suitable for studying open clusters. Details regarding the telescopes at the site will be presented in Section 3 later in this paper. To capitalize on the advantages of studying open clusters, ARIES, Nainital is conducting long-term photometric monitoring using 1-m class telescopes to examine pulsating variable stars in both young open clusters (Joshi et al. 2020a; Lata et al. 2023) and intermediate-age open clusters (Joshi

* E-mail: dileep@aries.res.in

et al. 2020b; Maurya et al. 2023). Additionally, we also perform long-term surveys for pulsating A- and F-type field stars (Ashoka et al. 2000; Martinez et al. 2001; Joshi et al. 2003, 2006, 2009, 2010, 2012, 2016b, 2017). We have recently augmented this exploration with space-based observations from extended *Kepler* mission (K2) and *Transiting Exoplanet Survey Satellite (TESS)* concerning field stars (Trust et al. 2021, 2023; Joshi et al. 2022b; Dileep, Joshi & Kurtz 2024; Sarkar et al. 2024). In this study, we integrate the space-based observations for open star clusters with the ground-based observations.

Similar to open star clusters, eclipsing binaries (EBs) provide an independent assessment of fundamental stellar parameters. They provide accurate measurements of stellar masses and radii through orbital dynamics and eclipse depths (Panchal et al. 2023). If one of the binary components is pulsating, the target becomes increasingly unusual. The examination of pulsations in EB components provides insights into the internal structure of the pulsating star, system evolution, and the influence of tidal forces inducing oscillations (Pigulski 2006; Murphy 2019; Lampens 2021). The existence of these unusual variable systems in open clusters serves as valuable test beds for validating various theoretical models for pulsation and stellar evolution.

We conducted a comprehensive ground- and space-based investigation of the intermediate-age open star cluster NGC 2126 (Gáspár et al. 2003). We utilized ground-based photometric observations from telescopes of varying diameters at ARIES, Nainital, low- to medium-resolution spectra, *TESS* Full Frame Images (FFIs), and *Gaia* Data Release 3 (DR3) data.

The manuscript is structured as follows. Section 2 delineates the sample selection, while Section 3 examines ground-based observations for the detection of variable stars. In Section 4, we ascertain the membership of the detected variables within the cluster, and in Section 5, we evaluate the cluster parameters. Subsequently, in Section 6, we examine the *TESS* light curves (LCs) for all stars and categorize the identified variables in Section 7. Ultimately, we present the modelling of the binary LCs in Section 8 and provide a summary of our findings in Section 9. We present our conclusions in Section 10.

2 SAMPLE SELECTION

We selected NGC 2126 (RA = 06^h02^m37^s.9, Dec. = +49°52′59″), which is an intermediate-age open star cluster hosting various pulsating stars located in the δ Scuti instability strip. The first CCD photometric study of the cluster was performed by Gáspár et al. (2003). Later, it was studied by Liu et al. (2012) and more recently Chehlaeh et al. (2018) presented new ground-based photometric observations for NGC 2126 and reported 11 variables, including 2 new δ Scuti variables. This makes this cluster as a potential target for asteroseismic investigation of pulsating variables of A and F type. Another reason that makes this cluster interesting is the presence of the EB V551 Aur, which shows pulsational variability on top of the eclipses. The membership of this star to the cluster will place strong constraints on its evolution and pulsation mechanism. All of the previous ground-based studies had limitations due to their short and discrete observations. Thus, aliasing and frequency resolution limit the accuracy of detected frequencies. Furthermore, NGC 2126 has one EB, UCAC4 700–043174, but there were insufficient data to model the system or report an orbital period (Chehlaeh et al. 2018). Thanks to the nearly continuous *TESS* observations spanning approximately a month in each sector, we can address the limitations due to lack of continuous data in ground-based observations. The

long and short cadence of *TESS* enables us to study both faint and bright targets of the cluster.

3 GROUND-BASED PHOTOMETRIC OBSERVATIONS

Time-series photometric observations for NGC 2126 were acquired in the *V* and *R* bands with the 1.3-m Devasthal Fast Optical Telescope (DFOT), Nainital, India (Joshi et al. 2022a). This telescope is equipped with a 2k × 2k CCD, and gives a field of view of about 18 × 18 arcmin² with a plate scale of 0.54 arcsec pixel⁻¹. For standardization of our targets, the standard field SA 98 of Landolt (1992) was also observed in *UBVRI* filters. For the pre-processing of the images, several bias frames and twilight flats were taken during the observing nights. We furthermore observed the cluster in the *V* and *R* bands during one more night using the 1.04-m Sampurnanand Telescope (ST), Nainital, India. This telescope is equipped with a 4k × 4k CCD, which gives a field of view of about 15 × 15 arcmin² (Yadav et al. 2022). The CCD was used in 4 × 4 binning mode to increase the signal-to-noise ratio (SNR); this gives a plate scale of 0.92 arcsec pixel⁻¹ after binning. Additionally, we also observed the pulsating EB V551 Aur in NGC 2126 for a couple of nights with the 3.6-m Devasthal Optical Telescope (DOT; Kumar et al. 2018). This telescope is equipped with a 4k × 4k CCD Imager that covers a field of view of 6.5 × 6.5 arcmin² (Pandey et al. 2018) and has a plate scale of 0.2 arcsec pixel⁻¹ after 2 × 2 binning. An overview with the details of the collected ground-based observations is given in Table 1.

The images were pre-processed with Image Reduction and Analysis Facility (IRAF) tasks: `zerocombine`, `flatcombine`, and `CCDPROC`. We applied the method of point-spread function (PSF) photometry to obtain the instrumental magnitudes for the stars in the target field; for this, we used the code `DAOPHOTII` by Stetson (1992).

The standard field SA 98 was used to convert the instrumental magnitudes to standard magnitudes. The following equations define the resulting transformations (Stetson 1987):

$$v = V + (2.064 \pm 0.005) + (0.071 \pm 0.005)(V - I) + 0.21Q, \quad (1)$$

$$b = B + (2.652 \pm 0.007) - (0.143 \pm 0.006)(B - V) + 0.32Q, \quad (2)$$

$$i = I + (2.446 \pm 0.008) - (0.036 \pm 0.007)(V - I) + 0.08Q, \quad (3)$$

$$r = R + (1.910 \pm 0.010) + (0.088 \pm 0.016)(V - R) + 0.13Q, \quad (4)$$

$$u = U + (4.641 \pm 0.010) - (0.090 \pm 0.011)(U - B) + 0.49Q, \quad (5)$$

where v , b , i , r , and u are the instrumental magnitudes; V , B , I , R , and U refer to the standard magnitudes; and Q is the airmass.

The search for variables in the cluster field was done based on the LCs obtained with 1.3-m DFOT. The *V*-band photometric LCs from each night were combined together and then phase-folded with the period that matches the first main peak in the Lomb–Scargle periodogram. The same period was used to phase-fold the combined *R*-band LCs to see any corresponding variations in the *R* band. The stars that showed brightness variation greater than three standard deviations with respect to the mean brightness, at least in the *V* band, were considered to be variable stars and were chosen for further analysis. The LCs for newly detected member variables from the ground are given in Fig. 1 and the field stars in Figs. A1–A5. We also list the detected dominant frequencies and the corresponding amplitudes of the field stars in Table A1.

Table 1. Observational log for NGC 2126. The telescopes used for multiband photometric observations and the date of observations are listed. Each of the columns named *V*, *R*, *U*, *B*, and *I* has entries of the form ‘number of frames × exposure time’.

Telescope	Date of observation	<i>V</i>	<i>R</i>	<i>U</i>	<i>B</i>	<i>I</i>
1.04-m ST	2023 Nov 22	119 × 50 s	119 × 50 s	–	–	–
1.3-m DFOT	2022 Oct 29	71 × 40 s	70 × 30 s	–	–	–
	2022 Oct 30	12 × 40 s	12 × 30 s	–	–	–
	2022 Nov 11	200 × 50 s	–	–	–	–
	2023 Feb 11	59 × 50 s	59 × 30 s	–	–	–
	2023 Feb 14	44 × 50 s	44 × 30 s	–	–	–
	2023 Feb 18	103 × 50 s	103 × 30 s	–	–	–
	2023 Feb 19	17 × 50 s	17 × 30 s	–	–	–
	2023 Oct 15	50 × 50 s	3 × 50 s	–	–	–
	2023 Nov 14	100 × 50 s	100 × 30 s	–	–	–
	2023 Nov 18	111 × 50 s	111 × 50 s	–	–	–
	2023 Dec 2	102 × 50 s	103 × 30 s	3 × 300 s	3 × 120 s	3 × 20 s
	3.6-m DOT	2021 Dec 13	12 × 300 s	–	–	11 × 100 s
		–	–	–	1 × 150 s	–
2021 Dec 14		12 × 100 s	–	–	9 × 200 s	–
		10 × 150 s	–	–	12 × 300 s	–
		1 × 300 s	–	–	–	–
2021 Dec 15		16 × 100 s	–	–	11 × 270 s	–
		11 × 80 s	–	–	12 × 160 s	–
	2023 Mar 28	50 × 50 s	–	–	–	–

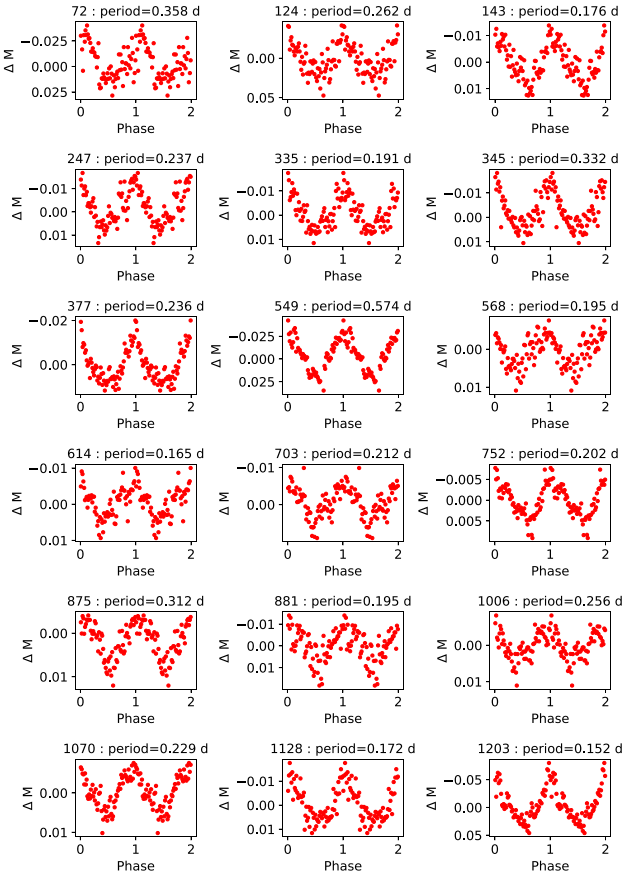


Figure 1. Phase-folded LCs of the newly detected variables, which are the members of open cluster NGC 2126. Their respective IDs and detected periods are given in the title of each plot.

4 CLUSTER MEMBERSHIP

For the determination of membership, we used astrometric data from *Gaia* DR3. The *Gaia* mission (Gaia Collaboration 2016) is an all-sky survey that collects multiband photometric, astrometric, and spectroscopic data. *Gaia*’s astrometric data have proven to be very successful in identifying and determining the membership of open clusters and globular clusters. The proper motion and parallax of all stars within a radius of 18 arcmin around the cluster centre were obtained by querying the *Gaia* DR3 catalogue (Gaia Collaboration 2023). Stars with large error bars were excluded from our study. We constructed the vector point diagram (VPD) of the cluster region to identify stars with similar proper motion (Fig. 2). Furthermore, we used the parallaxes to select samples with similar distances. For the membership probability, we used the method described in Wu et al. (2002) by identifying a cluster population and field population from the VPD. For this purpose, we plotted the radial density profile (RDP) of the VPD by calculating the number density in concentric annular regions from the centre of the VPD. For the centre of VPD, we smoothed the proper motion space with a 2D Gaussian kernel and chose the point with the maximum kernel density. The resultant RDP is shown in Fig. 3 along with a fitted King’s profile (King 1962). The number density was seen to approach the background density at a radial distance $\sim 0.8 \text{ mas yr}^{-1}$. We chose this as the limiting radius for probable cluster members and the stars outside this radius as field stars.

The *Gaia* colour–magnitude diagram (CMD) for stars having membership probability greater than 50 per cent is shown in Fig. 4. The members that are highly probable are situated along the main sequence, the evolved red giant branch, and the turn-off point. These members will introduce substantial constraints on the system’s age by means of isochrone fitting (see Section 5).

5 CLUSTER PARAMETERS

The CMD can be used to fit theoretical isochrones and determine cluster parameters such as age, metallicity, and reddening. The age and metallicity of the member stars should be comparable

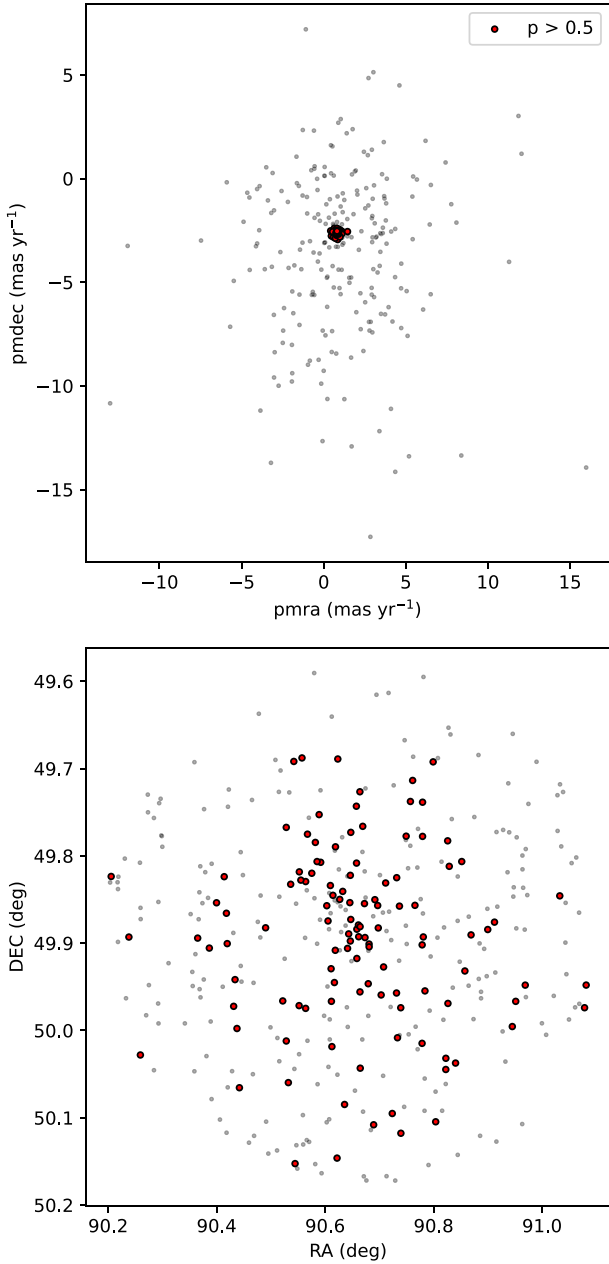


Figure 2. The top panel shows the VPD of NGC 2126 using *Gaia* DR3 proper motion data. The bottom panel shows the position of the cluster members and field stars in the sky as observed by *Gaia* DR3. Both panels have stars within an 18 arcmin radius from the centre, which was selected for membership determination. In both panels, the bold dots represent the member stars for which the membership probability is greater than 50 per cent and the faint dots in the background represent the field stars.

as a result of their shared origin. Thus, by comparing theoretical isochrones of varying ages and metallicities, we can estimate the cluster parameters. The *Gaia* CMD consists of the color index between *gaia* blue and red photometer bands (BP-RP colour) and the *G*-band mean magnitude. We used the isochrones downloaded from the CMD service [CMD 3.7](#) in the *Gaia* early data release 3 (*Gaia* EDR3) photometric system, and the evolutionary tracks from the PARSEC release v1.2S (Bressan et al. 2012; Chen et al. 2014, 2015; Tang et al. 2014). We utilized the *Gaia* DR3 parallaxes for the

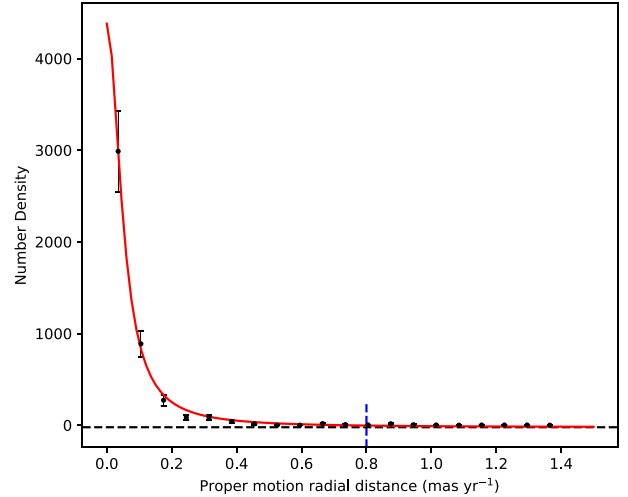


Figure 3. Number density plot for the proper motion space from *Gaia* data. The solid curve shows the best-fitting RDP. The horizontal dashed line shows the background density. The vertical dashed line marks the chosen limiting radius.

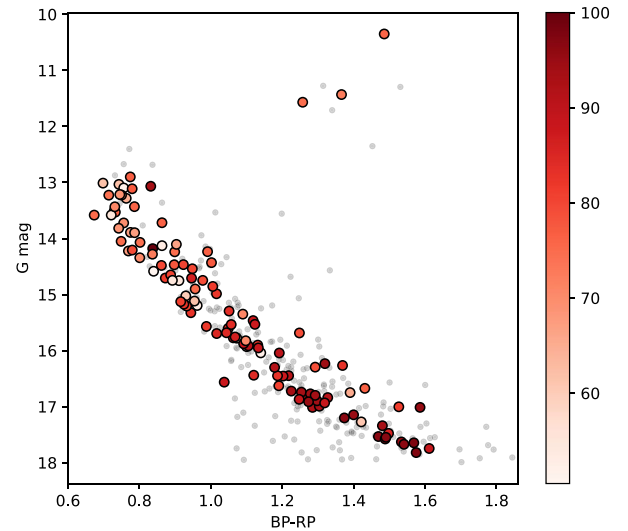


Figure 4. The CMD of NGC 2126 with the field stars (faint dots in the background) and the member stars (colour-coded bold dots according to their calculated membership probability). The probability scale is represented by the colour bar on the right side (50–100 per cent).

cluster members to determine an initial distance modulus and used prior literature values for an initial value for reddening. Utilizing these corrections, we drew a series of isochrones next to the observed CMD. Subsequently, the fit was optimized using the ASTECA code (Perren, Vázquez & Piatti 2015) by selecting the above guessed range of values (metallicity = [0.010, 0.030], log age = [9.0, 9.3], distance modulus = [9, 12], and extinction = [0.2, 1]) as uniform priors. ASTECA computes synthetic isochrones between the given grid of isochrones and uses a genetic algorithm (GA; Charbonneau 1995) to minimize the negative log likelihood, $-\log[L_i(z, a, d, e)]$, where z is the metallicity, a is the age, d is the distance, and e is the extinction. The GA is an optimization technique derived from natural selection, wherein a population of candidate solutions evolves over generations through selection (optimal fit), crossover (various combinations

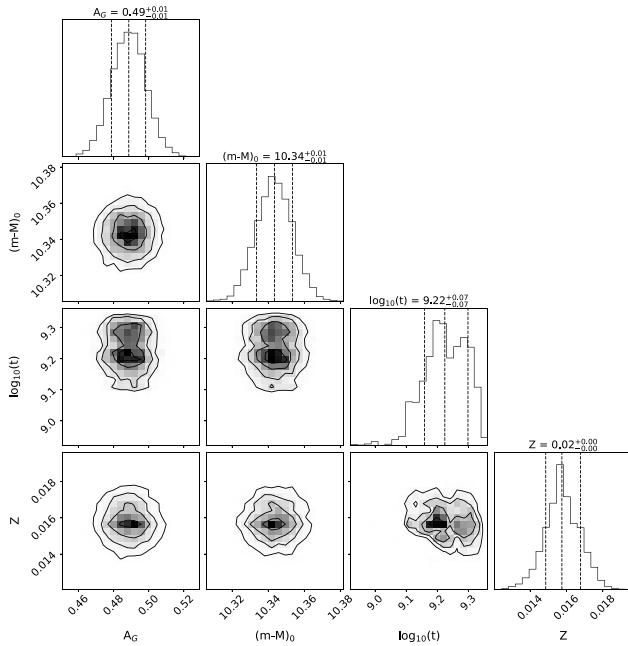


Figure 5. The resultant posterior distribution for the best-fitting isochrone.

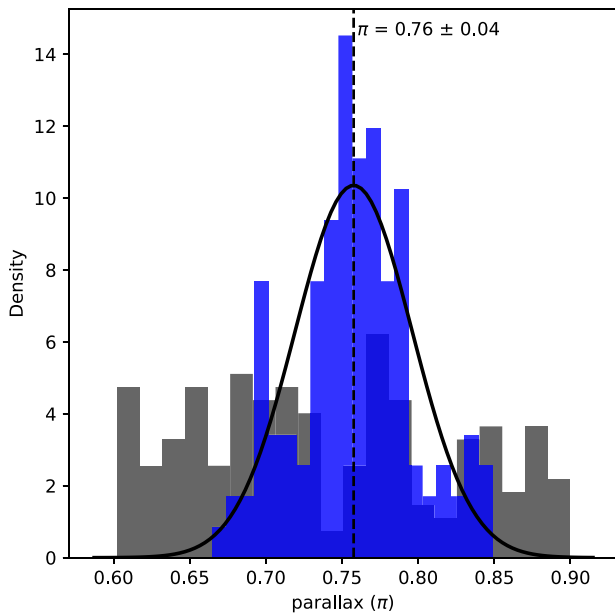


Figure 6. The histogram in blue displays the parallax distribution of the cluster members and the histogram in grey shows the parallax distribution of the field stars. By fitting a Gaussian to the cluster member parallaxes, we obtained the mean cluster parallax, which was then used to determine the distance to the cluster.

of parent sets), and mutation (random alterations introduced at each stage) to identify the most effective solution for a specific problem. It is particularly effective in exploring complex, multi-dimensional spaces and avoiding local minima. For more thorough details regarding the algorithm, please refer to Charbonneau (1995). Additionally, to quantify parameter uncertainties we employed the Markov chain Monte Carlo method within ASTECA; the resultant

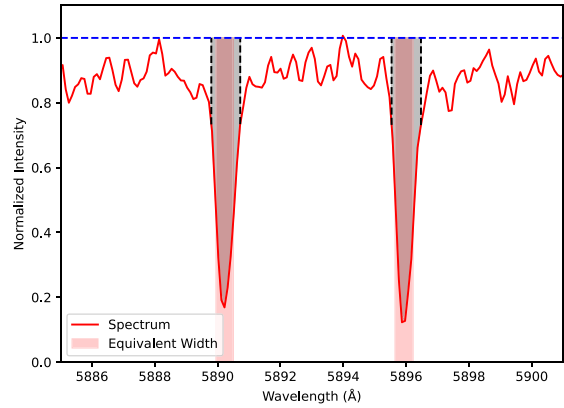


Figure 7. The interstellar absorption lines of sodium in the medium-resolution spectrum of V551 Aur. The blue horizontal dashed line is the continuum. We selected the regions between the vertical dashed lines to calculate the equivalent width of Na D1 and D2 lines, filled regions of absorption lines in the figure. The resultant equivalent width is the horizontal width of the filled rectangles drawn between 0 and 1.

Table 2. The table gives the best-fitting parameters for isochrone fitting with ASTECA. Here, Z is the metal fraction, t is the age in years, A_G is the extinction in *Gaia* G band, $(m - M)_0$ is the distance modulus of the cluster, D gives the distance to the cluster, and $E(B - V)$ is the reddening. The uncertainty in the last digit is given in brackets for each value.

Parameter	Isochrone fit	Parallax fit	Na D lines
$\log_{10}(t)$	9.22(7)	–	–
Z	0.016(1)	–	–
A_G	0.49(1) mag	–	–
$(m - M)_0$	10.34(1) mag	–	–
D	1.169(5) kpc	1.3(1) kpc	–
$E(B - V)$	0.20(4)	–	0.29(8)

posterior distribution is shown in Fig. 5. By fitting a Gaussian to the parallax histogram (Fig. 6), we calculated the mean parallax, which allowed us to calculate the distance to the cluster, which came out to be 1.3 ± 0.1 kpc. Also, we calculated distance to the cluster from the distance modulus of the isochrone fit using standard relations. We used the best-fitting coefficients published by *Gaia* team based on the empirical relation used by Danielski et al. (2018) to convert extinction in *Gaia* G band (A_G) to extinction in V band (A_V), and used $R_v = 3.1$ to get the reddening $E(B - V)$ for the cluster. We also verified this estimate using colour–colour diagrams from ground-based observations (Fig. B1). Apart from that, a medium-resolution spectrum (see Section 8.2) of a member variable, V551 Aur, was used to estimate the reddening towards the cluster. We used the calibration published by Poznanski, Prochaska & Bloom (2012), between the equivalent width of Na doublets and the reddening (Fig. 7). The final values for the Hertzsprung–Russell (HR) diagram were found by taking the average of the distance estimates from the isochrone fit and the parallax fit, as well as the reddening estimates from the isochrone fit and the Na doublets. The best-fitting parameters for the cluster are tabulated in Table 2 and the best-fitting isochrone is plotted in Fig. 8.

6 TESS PHOTOMETRY

The *TESS* is an all-sky survey telescope whose prime objective is to detect exoplanets orbiting nearby bright stars using the transit method

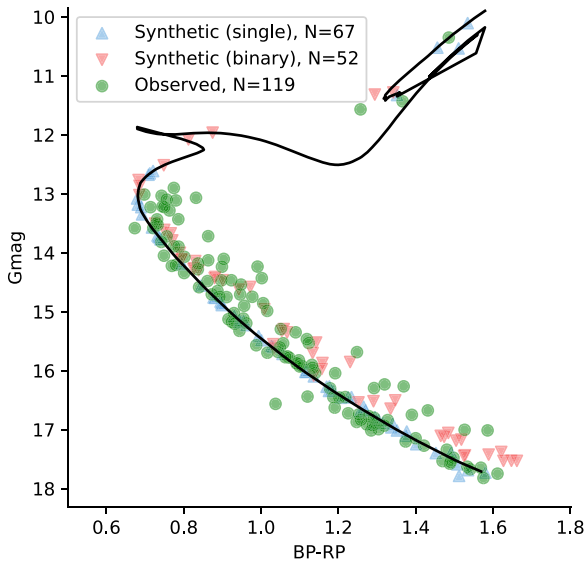


Figure 8. The figure shows the best-fitting isochrone using the code ASTECA represented by the solid curve. The synthetic members calculated by ASTECA are represented with straight and inverted triangles, respectively. Our input observed members from *Gaia* DR3 are represented as circles.

Table 3. NGC 2126 was observed in the sectors listed below. The observation period, cadence (in seconds), and duration (in days) are also given.

TESS sector	Observation period	Cadence (s)	Duration (d)
19	28 Nov–23 Dec, 2019	1800	24.5
59	26 Nov–23 Dec, 2022	200	26.4
73	7 Dec–3 Jan, 2024	200	26.9

(Ricker 2014). Apart from its primary mission, it also provides time-series photometry for asteroseismic studies of stars with magnitudes up to 12. *TESS* target pixel files (TPFs) and LC files are available with short cadences (20 and 120 s), while FFIs are taken with a longer cadence (30 min). Recently, the FFIs were taken at a shorter cadence of 200 s, which we used in our study. These data products can be downloaded from Mikulski Archive for Space Telescopes (MAST).

Given the large pixel size of the *TESS* CCD, which is 21 arcsec pixel⁻¹, resolving crowded fields like we see in open star clusters will be difficult, so our search for variability was primarily based on ground-based observations. The higher spatial resolution of ground-based observations enables the resolution of individual stars in the crowded field. Consequently, we concentrated our investigation of variability in the *TESS* FFIs on sources that had confirmed variable signals from the ground.

TESS observed the field of NGC 2126 during Sector 19 with an 1800-s cadence and during Sectors 59, 60, and 73 with a 200-s cadence. The observations from Sector 60 were excluded from this study because the targets were too close to the edge of the *TESS* CCD, preventing useful photometry. The log of observations taken from the *TESS* archive is given in Table 3. We performed the FFI photometry of our targets in the field using the PYTHON packages ELEANOR (Feinstein et al. 2019) and LIGHTKURVE (Lightkurve Collaboration 2018). To perform the photometry, we relied on the cut-outs taken from the FFI using the package TESSCUT (Brasseur et al. 2019).

ELEANOR is a PYTHON package that automates the extraction of LCs from FFIs. For Sector 19, the ELEANOR package was used and the resulting sky-subtracted LCs were free of telescope systematic and suitable for analysis. To identify our targets in the FFI, we overplotted the *Gaia* sources in the field and the apertures were carefully selected to reduce the contamination from nearby targets. ELEANOR did not perform well in Sectors 59 and 73, necessitating a manual approach utilizing the LIGHTKURVE package. Here, we also conducted an investigation into the FFI by overplotting the *Gaia* sources to minimize contamination from nearby sources and used custom apertures to extract the sky-subtracted LCs. As a final step, we used the RegressionCorrector in LIGHTKURVE package. The task creates a design matrix, which is a matrix of flux time series of the background pixels. For which a principal component analysis (Deb & Singh 2009) is performed to reduce its dimensionality and select the first few principal components, which contain most of the instrumental and systematic effects in that particular part of the sector. Then, a linear combination of these components is used to remove the long-term trends in the LC.

Furthermore, we attempted a global photometric search for variables in *TESS* FFIs independent of the ground-based observations with a PSF-based technique utilizing the flux distribution from *Gaia* observations, implemented in the PYTHON package TGLC (Han & Brandt 2023). We used TGLC for only long-cadence data (Sector 19), since the computational expense for short cadence was high and not possible for us at the moment. This resulted in the discovery of one new variable in addition to the known variables. Due to contamination-related uncertainty, we had to discard a lot of other targets with variable signals. We discuss how we dealt with the effect of contamination in our data in Section 6.1.

The frequency analysis for the variable stars in *TESS* data was done using the program PERIOD04 (Lenz & Breger 2004). We adopted the criterion SNR ≥ 5.6 given by Zong et al. (2016) for space-based observations. The SNR was calculated after pre-whitening all of the dominant frequencies to obtain the residual spectra, followed by calculating the noise using a box size of one cycle per day along both sides of the target frequency. The errors in frequency and amplitude were calculated using the analytical relations provided by Montgomery & O’Donoghue (1999). Tables C1 and C2 list the frequencies for the known variables detected using *TESS* and from the ground and the LCs in the respective sectors are plotted in Figs C1, C2, and C3.

6.1 Contamination

The large pixel size of *TESS* causes the blending of signals from nearby sources. The resulting LCs for a target can only be trusted when (i) the source is much brighter than the nearby contaminating sources so that the background source only adds to the noise and (ii) the contaminating sources are non-variables and, hence, only increase the noise level rather than introduce signals in the periodogram.

In order to investigate the contamination in *TESS* LCs, we first overplotted the *Gaia* sources on the TPF in the vicinity of each target to see whether there are any bright nearby objects that might potentially contribute to contamination. After that, we selected a variety of custom apertures to determine the origin of a specific set of frequencies within the frequency spectrum. An example of this investigation is shown in Fig. 9, where V551 Aur (V6) is a pulsating EB that is contaminated with a δ Scuti star (N1). Next, we cross-checked whether any of these frequencies are pre-defined in the ground-based data obtained from Chehlaeh et al. (2018). For

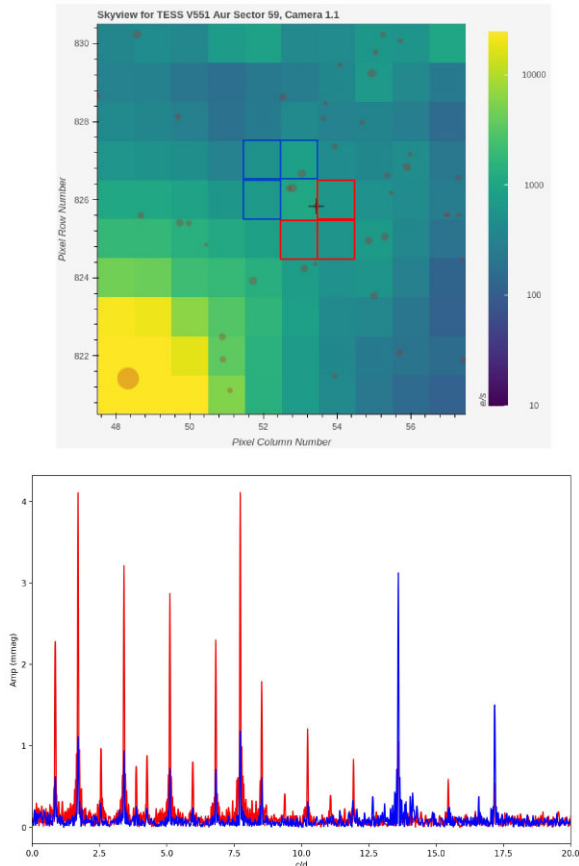


Figure 9. The top panel depicts the TPF of star V6 overlaid with nearby *Gaia* DR3 targets. V551 Aur (V6) is identified with a ‘+’ symbol. Custom apertures were chosen near V6 (marked with red boxes) and N1 (marked with blue boxes). The bottom panel depicts the periodogram generated by the two apertures, V6 in red and N1 in blue, which are superimposed on each other. The harmonic signals and pulsation are stronger in the red aperture and weaker in the blue aperture. The two dominant frequency signals in blue behave in opposite ways, indicating that they are from the nearby star N1.

example, in case of V6 in Fig. 9, the two strong blue peaks towards the right were detected by Chehlaeh et al. (2018) for N1 and few of the dominant red peaks to the left were reported by Chehlaeh et al. (2018) for V6.

We found that two of the pulsating stars ZV2 (hybrid star) and N1 (δ Scuti star) were contaminated significantly by the nearby binary stars V4 and V6, respectively, and found that the contamination can be addressed with the above technique. Furthermore, to quantify the extent of contamination endured by the variable stars detected in our study, we calculated a contamination factor for each of these stars using *Gaia* DR3 positions and magnitudes, where we took the ratio of the target flux to the total flux in a 21 arcsec radius.

7 CLASSIFICATION OF VARIABLE STARS

Variable stars are classified according to the shape of their LCs, amplitude of variability, frequency of variability, and location on the HR diagram. The pulsating stars can be identified from the HR diagram by plotting the instability strips for δ Scuti and γ Doradus pulsator. In our study, we used the theoretical δ Scuti and γ Doradus instability strips, computed by Dupret et al. (2005).

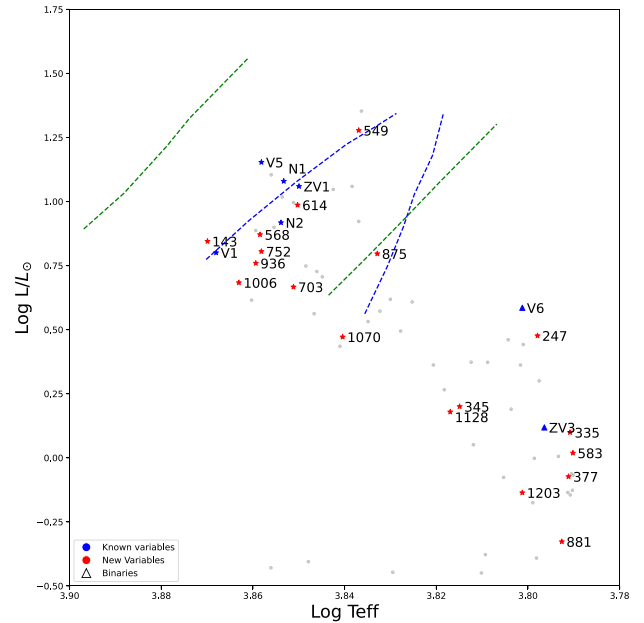


Figure 10. HR diagram for the member stars based on the ground-based observations. Blue ‘star’ symbols and the blue triangles indicate the known pulsating variables and the EBs, respectively. The red ‘star’ symbols represent the newly detected variable stars. The green and blue dashed lines represent the edges of the theoretical δ Scuti and γ Doradus instability strips, respectively, computed by Dupret et al. (2005).

The standard *B*- and *V*-band magnitudes from our ground-based observations with the 1.3-m DFOT were used to generate the HR diagram for the cluster members. After extinction correction, the colour index, which is the difference between *B*-band magnitude and *V*-band magnitude (*B*-*V*), was used to find the effective temperature (T_{eff}), which was based on an empirical relationship from Torres (2010). Next, the empirical relation provided by Torres (2010) was employed to calculate the bolometric correction (BC_V) for the stars in the *V* band. Then, the luminosity can be estimated using the standard relations, where we took bolometric magnitude of sun as $M_{\text{bol},\odot} = 4.73$ (Torres 2010). The HR diagram in Fig. 10 shows the known variables, the newly found variables, and the instability strips for the δ Scuti and γ Doradus pulsations.

γ Doradus variables are mainly non-radial g-mode pulsators showing periodic variations in their brightness with pulsation frequencies ranging from 0.5 to 3 d⁻¹ (Aerts, Christensen-Dalsgaard & Kurtz 2010) and amplitude of variation up to 0.1 mag in the *V* band. The convective blocking drives the g-mode pulsations, with buoyancy as the restoring force (Dupret et al. 2005). In the HR diagram, the γ Doradus instability strip is seen overlapped with the cooler edge of the δ Scuti instability strip in the main sequence with an early F spectral type.

δ Scuti stars are primarily p-mode pulsators with brightness variations ranging from 0.001 to 0.8 mag in the *V* band and pulsation frequencies ranging from 5 to 50 d⁻¹ (Aerts et al. 2010). The κ -mechanism drives the pulsations in these stars, which occur at the partial ionization zones in the outer radiative region (Pamyatnykh 2000). These stars are found at the lower part of the classical instability strip, which intersects the main sequence, called the δ Scuti instability strip. They are A- to early F-type stars with masses ranging from 1.5 to 2.5 M_{\odot} . They pulsate in both radial and non-radial p modes. Some of the stars pulsate both in g modes and p

Table 4. The newly detected variable cluster members are listed with their ID, RA, Dec., standard magnitude, first dominant frequency used for phase folding, corresponding semi-amplitude, assigned variability type, membership, and contamination in *TESS*.

ID	RA (deg)	Dec. (deg)	Mag (mag)	Frequency (d^{-1})	Amp (mag)	Variability type	Mem. (per cent)	Cont. (per cent)
72	90.5885	49.752 833	17.423	2.796	0.022	–	90.8	49.40
124	90.527 917	49.767 417	18.18	1.905	0.029	–	85.8	0
143	90.567 028	49.775 222	13.817	5.690	0.009	DSCT	75.2	0
247	90.657 528	49.808 472	14.785	4.224	0.010	–	77.3	33.17
335	90.711 278	49.831 306	15.739	5.234	0.009	–	70.9	3.79
345	90.536 139	49.832 639	15.455	3.016	0.009	–	61.9	3.44
377	90.607 278	49.842 75	16.169	4.231	0.011	ROT	57.3	89.78
549	90.663 472	49.881 278	12.743	1.741	0.024	–	89.8	51.58
568	90.606 944	49.884 222	13.752	5.119	0.005	DSCT	54.9	89.35
614	90.643 167	49.889 639	13.465	6.062	0.006	DSCT	64.8	46.79
703	90.680 778	49.901 25	14.264	4.722	0.005	–	74.4	37.33
752	90.6185	49.908 417	13.916	4.948	0.005	–	69.8	20.28
875	90.610 778	49.929 528	13.949	3.202	0.005	GDOR	76.3	7.07
881	90.857 528	49.932 306	16.802	2.568	0.008	ROT	83.1	38.97
1006	90.611 389	49.966 889	14.22	3.906	0.005	–	74.8	1.89
1070	90.679 444	49.983 611	14.756	4.359	0.005	–	50.5	3.21
1128	90.437 278	49.997 917	15.505	2.907	0.012	–	82.7	24.59
1203	90.778 667	50.015 194	16.312	3.284	0.055	ROT	90.2	3.19

Notes. DSCT: δ Scuti, GDOR: γ Doradus, and ROT: Rotational variable.

Table 5. The variables detected in *TESS* with their IDs, names (if any), the orbital or rotational period [P (d)] from *TESS*, the pulsational period [P_{pul} (d)] from *TESS*, assigned variability type, membership from *Gaia* DR3 (Mem.), and *TESS* contamination (Cont.). The error values at the last digit are represented inside brackets for the periods.

ID	Name	RA	Dec.	P (d)	P_{pul} (d)	Variability type	Mem. (per cent)	Cont. (per cent)
V1	V546 Aur	90.433 639	49.941 861	–	0.8094(2)	GDOR	68.7	0.24
V2	V547 Aur	90.488 972	49.982 056	–	0.9394(2)	GDOR	–	0.37
V3	V548 Aur	90.521 556	49.819 861	–	0.078 040(6)	DSCT	–	6.38
V4	V549 Aur	90.588 583	49.877 167	3.300 284(1)	–	EB	–	88.50
V5	V550 Aur	90.609 806	49.865 889	–	0.082 706(7)	DSCT	–	7.36
V6	V551 Aur	90.658 250	49.884 250	1.173 1767(4)	0.129 453(8)	EB + DSCT	76.5	88.52
ZV1	UCAC4 700–043212	90.637 472	49.880 111	–	0.081 61(1)	DSCT	51.6	15.05
ZV2	UCAC4 700–043178	90.590 278	49.873 361	–	0.067 336(9)	Hybrid	–	38.08
ZV3	UCAC4 700–043174	90.584 750	49.806 611	3.224 040(2)	–	EB	83.7	59.84
N1	UCAC4 700–043245	90.661 139	49.879 417	–	0.073 534(4)	DSCT	61.8	65.29
N2	UCAC4 700–043196	90.614 056	49.845 361	–	0.068 719(9)	DSCT	70.7	10.51
839	–	90.648 306	49.920 833	0.7390(3)	–	ROT	–	2.17

Notes. DSCT: δ Scuti, GDOR: γ Doradus, EB: Eclipsing binary, and ROT: Rotational variable.

modes, with characteristics similar to γ Doradus and δ Scuti stars. These stars are known as hybrid pulsators (Handler et al. 2009).

The G- and K- spectral type stars are located below the δ Scuti and γ Doradus instability strips. These stars, with a convective envelope, exhibit rotational variability due to spots on their surface (Mamajek & Hillenbrand 2008). The LCs of these rotational variables produce a frequency spectrum with the rotational frequency below 5 d^{-1} and at least one harmonic of the rotational frequency (Balona 2013). Thus, we classified the main-sequence variables with a frequency less than 5 d^{-1} falling in the G to K spectral type as rotational variables. Also, in this region one can find the solar-type oscillations. The stars whose LCs show (partial or full) eclipses can be classified as EBs.

All of the member stars, as well as those with LCs in both *TESS* and ground-based observations, were classified according to the criteria listed above. Table 4 shows the results for newly discovered member stars, while Table 5 shows the results for stars with variability in *TESS* and ground-based observations. We observe that ground-based classification is incomplete due to insufficient data.

7.1 Intrinsic variables

7.1.1 γ Doradus stars

NGC 2126 contains two known γ Doradus variables (V1 and V2). Our membership analysis revealed that V2 is not likely to be a cluster member. The two stars were detected by *TESS*. Both stars have a frequency lower than 3 c/d. Fig. 11 shows a comparison of our results with previous frequency estimates from the literature. There were no harmonics of the fundamental frequency in the frequency spectrum, showing that they are not rotational variables. The position of V1 in the HR diagram is within the γ Doradus instability strip. Since V2 is not a member star, we used the *Gaia* temperature $T_{\text{eff}} = 7134 \text{ K}$, indicating that it is an early F-type star. Thus, we classify V1 and V2 as γ Doradus variables. From our ground observations, we classified the star 875, as γ Doradus variable, based on the frequency and position in the HR diagram. The *TESS* data for this star produced null results.

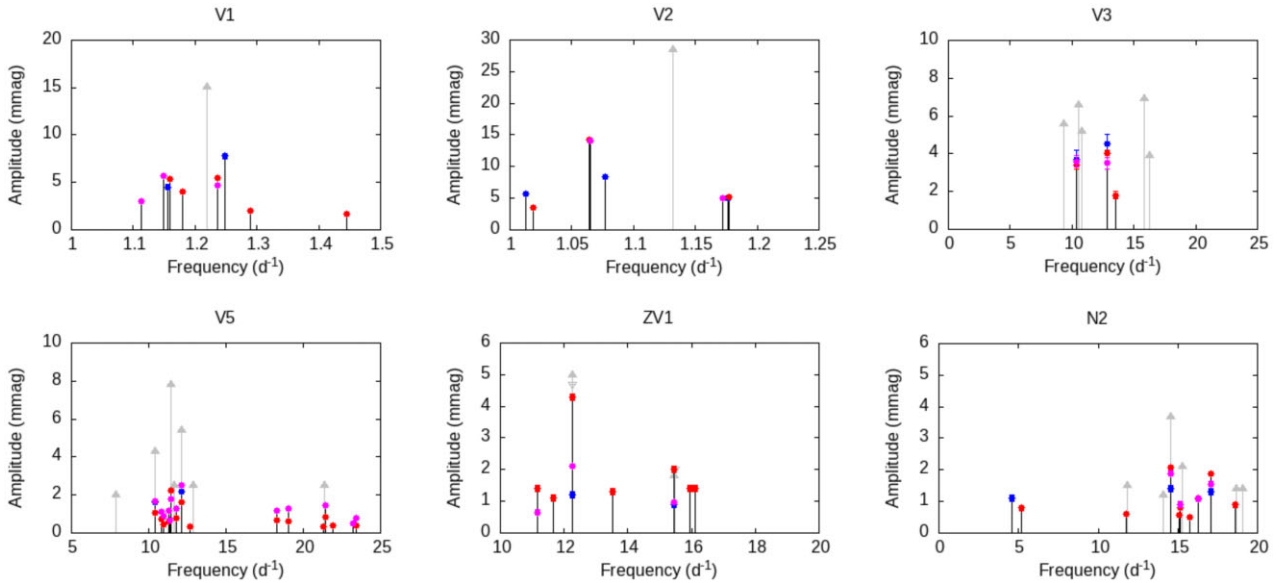


Figure 11. Representation of the results of the frequency analysis of the *TESS* data of the stars without contamination. The filled circles with error bars in blue, red, and magenta show the observed amplitudes in the *TESS* data of Sectors 19, 59, and 73, respectively. They are compared to those published by Chehlaeh et al. (2018) (upward triangles) and Zhang, Deng & Luo (2012) (downward triangles), if available.

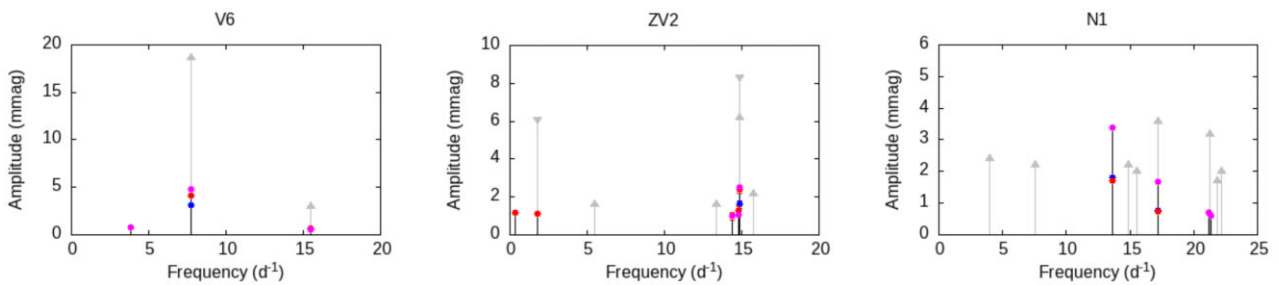


Figure 12. Same as Fig. 11, but for stars affected by contamination.

7.1.2 δ Scuti stars and hybrid pulsators

Chehlaeh et al. (2018) reported five δ Scuti stars (V3, V5, ZV1, N1, N2) and a hybrid pulsator (ZV2). All of these stars were detected in *TESS* data. ZV1, N1, and N2 were determined to be probable cluster members. Figs 11 and 12 show a comparison between the frequencies detected in literature and those we detected from *TESS*'s three sectors. Pulsation frequencies in ZV1, N1, and N2 were similar to those of a δ Scuti star, ranging from 5 to 30 c/d. They belong to the δ Scuti instability strip on the HR diagram. Thus, we classify these stars as δ Scuti stars. However, N1 is contaminated by a nearby binary star V6. To address this, we used the method described in the previous section. Since V3 and V5 are not cluster members, we used the *Gaia* temperatures; V3 has $T_{\text{eff}} = 7454$ K, while V5 has $T_{\text{eff}} = 6166$ K, which corresponds to a spectral type F. The spectral type along with the pulsation frequencies from *TESS* indicates that these are δ Scuti stars. According to Zhang et al. (2012), ZV2 is a hybrid pulsator because it has a low frequency of 1.812 d^{-1} in addition to the δ Scuti-type frequencies. Our analysis of *TESS* data recovered the dominant frequency 14.851 d^{-1} , as well as the low frequency reported by Zhang et al. (2012). As ZV2 is not a member, we used the *Gaia* temperature, $T_{\text{eff}} = 7081$ K, indicating an F-type star. This means that the star is in the γ Doradus instability strips where δ Scuti instability strip also overlaps. Thus, we classify it as a

hybrid pulsator. This star was also contaminated by a nearby EB, V4. We used the method described in previous section in this case also to identify the frequencies. Using ground-based data, we identified three new δ Scuti variables, 143, 568, and 614. The classification was made based on their positions in the HR diagram and oscillation frequencies. *TESS* detected no signals from these stars due to high contamination.

7.2 Extrinsic variables

7.2.1 Rotational variable

We discovered a new variable, 839, in the field of NGC 2126. The star shows variable signals on the ground, as well as *TESS* data. Fig. 13 compares the *TESS* LC and frequency spectra of this star. This star demonstrates *TESS*'s improved frequency resolution. The dominant frequency is the same in both spectra; however, the ground-based spectrum has many aliases. The frequency is less than 5 c/d and appears as harmonics in the *TESS* frequency spectra. The *Gaia* temperature, $T_{\text{eff}} = 5725$, indicates a G-type star. Thus, we classify this star as a rotational variable. From the ground-based observations, we also identified three additional rotational variables, 377, 881, and 1203. We were unable to detect any of these stars using *TESS* due to contamination.

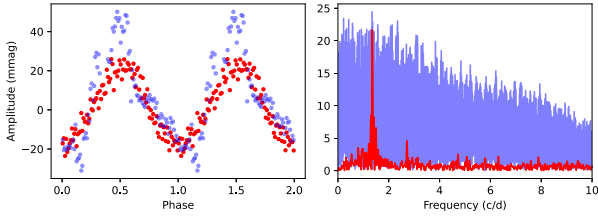


Figure 13. The left panel shows the LCs for the newly detected rotational variable 839 phase-folded to the dominant peak in its frequency spectrum and binned with a bin size of 0.02 in phase. The red points are from *TESS* Sector 19 and the blue points are from the ground-based observations. In the right panel, the corresponding frequency spectra for the respective LCs are given. We see the advantage of frequency resolution from *TESS* compared to the ground-based observations.

7.2.2 Eclipsing binaries

Chehlaeh et al. (2018) identified three EBs in NGC 2126, V4, V6, and ZV3. They were able to cover a large enough phase range for two stars, V4 and V6, allowing them to model the LCs and derive basic parameters such as orbital periods, inclination, mass ratio, and temperature ratio. For ZV3, however, modelling and period determination were not possible due to a lack of data covering the full eclipse. We used continuous time-series *TESS* observations to fully cover the three EBs' phase range in our study. ZV3 and V6 are members of the cluster, while V4 is not a member. Given the cluster membership, the case of V6 is more interesting because it is a pulsating EB.

According to available data, Chehlaeh et al. (2018) estimated an orbital period of 1–1.5 d for ZV3. However, with the help of *TESS* data that included multiple eclipses, we were able to calculate the orbital period for this star. We used all of the primary minima found in Sectors 19, 59, and 73 by fitting a parabola to their dips. To determine the system's linear ephemeris, the orbital cycle versus time of primary minima (TOM) curve was fitted with a linear relation.

The resulting linear ephemeris for ZV3 is

$$\text{BJD}_{\min} = 2458818.0594 \pm 0.0008 + 3.224040 \pm 0.000002 \times E, \quad (6)$$

where BJD_{\min} is the time of primary minima at epoch E . Fig. 14 shows the ephemeris fit.

For V4, Chehlaeh et al. (2018) discovered an orbital period of 3.300 281 d. We collected LCs for this star from *TESS* Sectors 19, 59, and 73. In addition to the primary minima detected from *TESS* sectors, two minima reported in Chehlaeh et al. (2018) were included in the ephemeris fit.

The subsequent linear ephemeris for V4 is

$$\text{BJD}_{\min} = 2452308.388 \pm 0.002 + 3.300284 \pm 0.000001 \times E. \quad (7)$$

Gáspár et al. (2003) described V6 as an EB with a pulsating component. Chehlaeh et al. (2018) revisited the nature of this variable star, as well as the parameters of the open cluster that hosts it. They concluded that the pulsation could be caused by tidally excited g modes, which exhibit tidal resonance with the orbital period. Although previous research concluded that V551 Aur is unlikely to belong to the open cluster, our analysis of *Gaia* DR3 data revealed that it most likely does. As in the previous case, we determined the linear ephemeris from all the primary minima detected in *TESS*

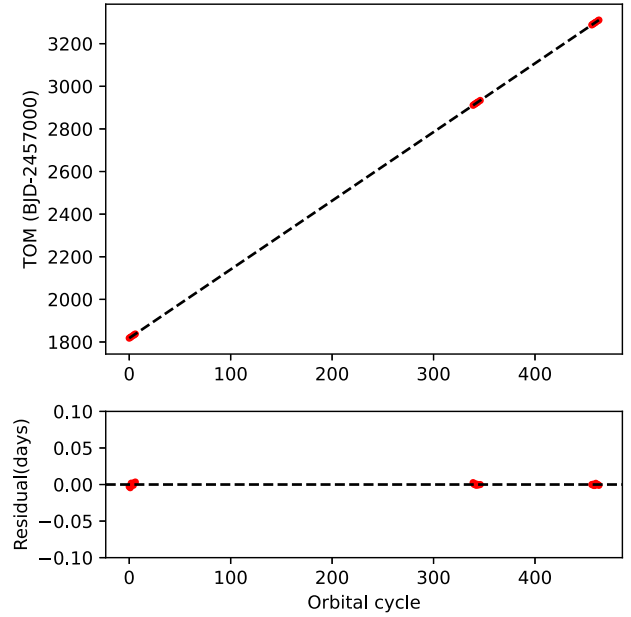


Figure 14. The top panel shows the orbital cycle versus TOM detected from all the three *TESS* sectors. The dashed line is the straight line fit to these data. The bottom panel shows the residuals of the fit.

sectors, as well as the ground-based minima listed in table 9 of Chehlaeh et al. (2018).

The final linear ephemeris for V6 is

$$\text{BJD}_{\min} = 2452307.410 \pm 0.003 + 1.1731767 \pm 0.0000004 \times E. \quad (8)$$

Fig. 15 depicts the phased and binned *TESS* LCs for three EBs. Figs D1 and D2 show the ephemeris fit for V6 and V4, respectively.

8 ECLIPSING BINARY MODELLING

EBs provide an independent method for calculating stellar masses and radii. By modelling the eclipsing LCs and the radial velocity curve, we can determine the best-fitting parameters for masses, radii, inclination, and so on. However, we only have *TESS* LCs for our EBs. Due to the faintness of these stars, no high-resolution spectra could be obtained using the facilities we have direct access to. Thus, we used the eclipsing LCs alone to model our EBs. While modelling the EB LC, one should take care of the intrinsic variability that it may possess due to either some intrinsic process in the system such as pulsations, mass transfer, star-spots, etc. (Pigulski 2006) or external reasons such as telescope systematics or contamination in case of *TESS*. Therefore, it was imperative to incorporate the intrinsic variability or long-term systematics into the LC modelling process.

The primary and secondary minima of all three of our EBs (V4, V6, and ZV3) are clearly distinct, with the out-of-eclipse region flat and the secondary minima precisely located at the 0.5 phase of the orbital period. Consequently, it is reasonable to assume that they are detached binaries in a circular orbit. We modelled the intrinsic variability in EB LCs using the CELERITE package (Foreman-Mackey et al. 2017; Foreman-Mackey 2018). This package is part of the EXOPLANET¹ package (Foreman-Mackey et al. 2021) and

¹<https://github.com/exoplanet-dev/exoplanet>

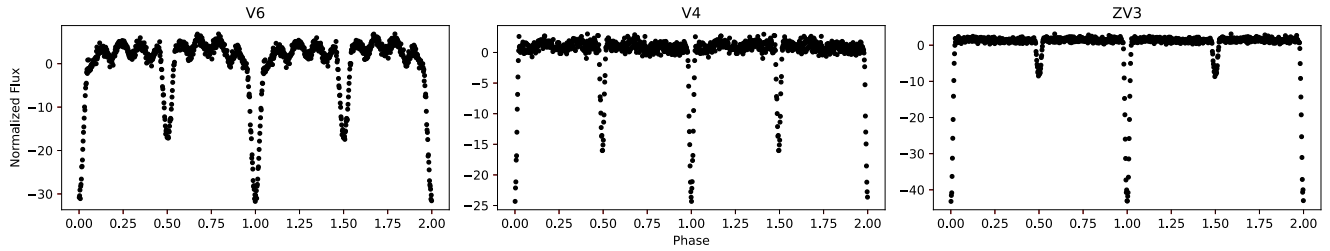


Figure 15. From left to right, each panel shows the phased LCs of V6, V4, and ZV3, using all the available *TESS* sectors (19, 59, and 73) and binned using a bin size 0.002 in phase. For V6, we can clearly see the pulsations on top of the eclipses.

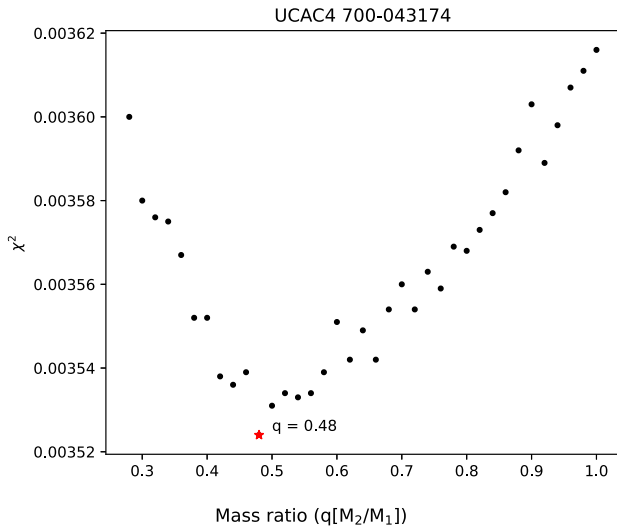


Figure 16. The figure shows the q (mass ratio) search for UCAC4 700–043174 (ZV3) using PHOEBE 1.0 legacy version. The q value with minimum χ^2 is marked with an asterisk and was chosen for further modelling.

features a scalable Gaussian process model with a SHOTERM (a term representing a stochastically driven, damped harmonic oscillator). This package has the capability to simultaneously model the intrinsic variability with a scalable Gaussian process and the eclipses for a detached binary system. The EXOPLANET code employs PYMC (Fonnesbeck et al. 2015) for its probabilistic modelling. It utilizes the STARRY package (Luger et al. 2019) to generate limb-darkened LCs and employs a fast and efficient solver for Kepler’s equations.

The q -search method (Wilson 1994; Joshi, Jagirdar & Joshi 2016a) can be employed to estimate the mass ratio (q -value) of the system in the absence of spectroscopic data. Previous studies by Liu et al. (2012) and Chehlaeh et al. (2018) calculated the mass ratio for V6 and V4, respectively, using the photometric q -search method using the PHOEBE 1.0 legacy version based on Wilson–Devinney code (Prša & Zwitter 2005). We used the q -values calculated for V4 and V6 from previous studies. For ZV3, we used a similar approach and calculated the q -value with PHOEBE 1.0. The best-fitting q -value was $q = 0.48$ based on the q -value versus chi-square plot, as shown in Fig. 16.

These photometrically derived q -values served as priors for modelling the EB LCs. The primary star’s mass was determined by comparing evolutionary tracks on the HR diagram, and the radius was calculated using the Stefan–Boltzmann’s relation, with the primary star’s temperature being the B–V colour temperature in the case of V4 and ZV3. For V6, we used the spectroscopic temperature obtained through medium-resolution spectroscopy.

Table 6. The parameters computed with EXOPLANET code for ZV3, V4, and V6 are given in the table. T_0 is the time of primary minima, q is the mass ratio, i is the inclination, k is the radius ratio, e is eccentricity, and s is the surface brightness ratio. The last two terms are the Gaussian process parameters, ρ_{gp} represents the undamped period of the oscillator and σ_{gp} is the standard deviation of the process.

Star	Parameter	This work	Chehlaeh et al. (2018)
ZV3	Period (d)	3.224 040 (fixed)	–
	T_0 (BJD)	2458818.0594 (fixed)	–
	q	0.480(5)	–
	i (deg)	82.10(9)	–
	k	1.0(2)	–
	e	0.04(4)	–
	s	0.20(9)	–
	ρ_{gp}	1.0(2)	–
	σ_{gp}	1.7(2)	–
V4	Period (d)	3.300 284 (fixed)	3.300 281(1)
	T_0 (BJD)	2452308.388 (fixed)	–
	q	0.626(6)	0.626(7)
	i (deg)	80.4(2)	86.61(6)
	k	0.6(2)	–
	e	0.13(5)	0 (fixed)
	s	2(1)	–
	ρ_{gp}	0.23(2)	–
	σ_{gp}	4.9(2)	–
V6	Period (d)	1.173 1767 (fixed)	1.173 1752(8)
	T_0 (BJD)	2452307.410 (fixed)	–
	q	0.769(8)	0.769(5)
	i (deg)	61.8(7)	73.01(6)
	k	0.90(9)	–
	e	0.02(1)	0 (fixed)
	s	0.8(2)	–
	ρ_{gp}	0.116(5)	–
	σ_{gp}	5.3(2)	–

Table E1 contains the prior distributions that were chosen for modelling in the EXOPLANET code. Table 6 provides the best-fitting parameters for binary modelling for all stars, which were compared to previous estimates by Chehlaeh et al. (2018). Figs 17, 18, and 19 depict the best-fitting LCs. Figs E1, E2, and E3 and Figs 20, E4, and E5 show the Gaussian process fits and corner plots, respectively.

8.1 V551 Aur: a pulsating eclipsing binary

V551 Aur is an EB that exhibits pulsational variability in its LC. Previous authors proposed that the variability could be due to pulsations in the binary system’s primary component. However, the

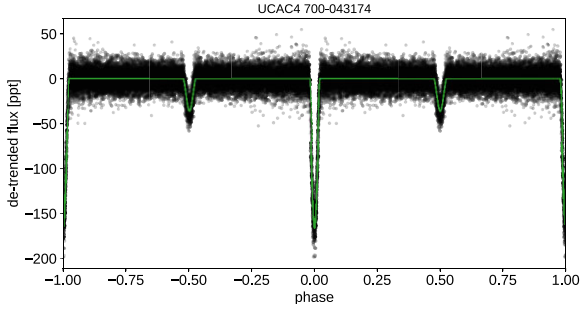


Figure 17. The phase-folded LC of UCAC4 700–043174 (ZV3) with the best-fitting model.

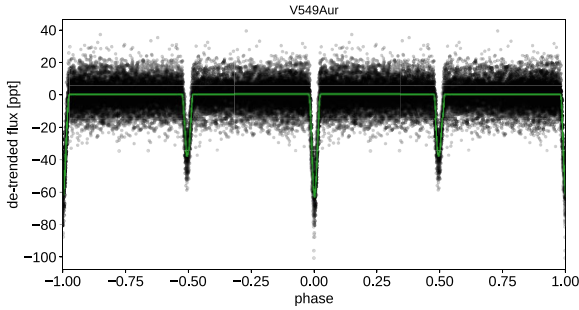


Figure 18. The phase-folded LC of V549 Aur (V4) with the best-fitting model.

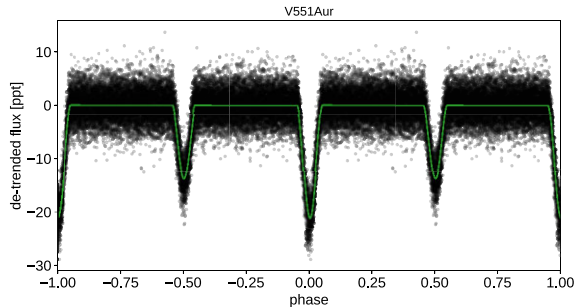


Figure 19. The phase-folded LC of V551 Aur (V6) with the best-fitting model.

nature and origin of this star’s pulsation remain poorly understood. The associated frequency, $7.7248(5)$, is very close to the 9th harmonic of the orbital frequency, so the pulsation may be a higher order resonance with the orbital frequency. This could indicate a tidally excited g mode on the primary star. The companions’ nature is unknown because no spectroscopic observations have been made.

As described in the previous section, we modelled both eclipses and intrinsic variability simultaneously. The pulsational frequency, first harmonics, second harmonics, and sub-harmonics were identified in the residuals of the eclipse model subtracted LC (refer to Fig. 21). The presence of a sub-harmonic frequency in the pulsation indicates that the pulsations are non-linear, which is not expected from a pure stable oscillator. This lends credence to the theory that the pulsation in one of the companions is caused by tidal forces. The ground-based phased LC (Fig. 22) shows that during the secondary

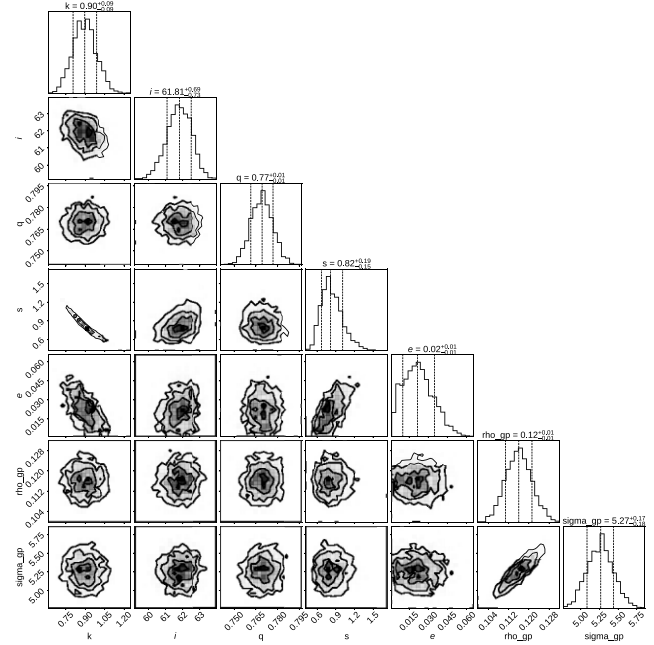


Figure 20. The resultant posterior distribution for the eclipse model and the Gaussian process model for the best fit from EXOPLANET code for V551 Aur.

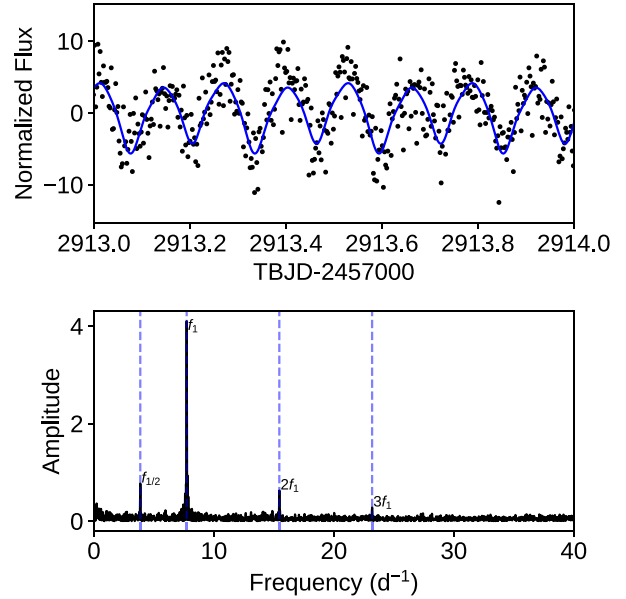


Figure 21. The top panel shows the residuals after removing the binary model from the LC of V551 Aur. Here, only the pulsation signals are seen. The bottom panel shows the frequency spectrum of the residual. Apart from the dominant peak being the pulsation frequency, one can notice the first two harmonics and a sub-harmonic in the spectrum.

eclipse, pulsations dominate, indicating that the pulsating member is the primary companion.

8.2 Spectroscopy

Low-resolution spectroscopic observations for V551 Aur were carried out with Himalayan Chandra telescope (HCT), Hanle Faint

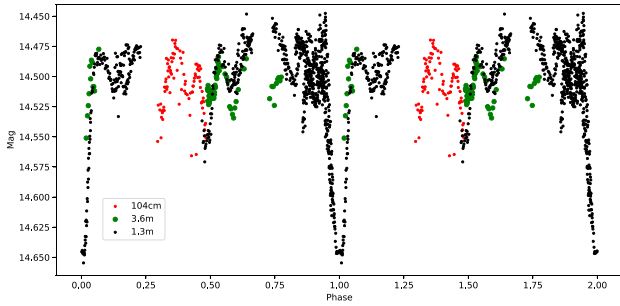


Figure 22. Ground-based phase-folded LC of V551 Aur using the orbital period determined from *TESS*. The red, green, and black data points represent the data taken with 104-cm Sampurnanand, 3.6-m DOT, and 1.3-m DFOT telescopes, respectively, at ARIES, Nainital.

Object Spectrograph Camera (HFOSC; Cowsik, Srinivasan & Prabhu 2002), during 2021 and 2022. A total of 16 spectra with a resolution of $R \sim 1200$ were obtained during different phases of the orbital period. The radial velocities proved to be unreliable for our study because of the low resolution and due to the fact that the components' profiles are always blended and furthermore affected by the pulsation. However, close examination of the strong Balmer lines shows significant line profile variations across different phases (see Fig. 23 for the $H\alpha$ lines) indicating a spectroscopic binary. A series of high-resolution spectra is required to construct the star's radial velocity curves, which will provide accurate system parameters. Because we do not have direct access to the spectroscopic observational facilities required to observe a 14th magnitude star, we propose this as a future project. We used the low-resolution spectra to determine the basic parameters of the star by comparison with synthetic spectra (Table F1), using the chi-square minimization technique employed in GSSP code (Tkachenko 2015).

A medium-resolution spectrum was taken with the 2.4-m telescope, Thailand National Observatory, Thailand, Medium-Resolution Spectrograph with a resolution of $R \sim 18000$ over a range of 380–900 nm. The $H\beta$ line (Fig. 24) was used to calculate the T_{eff} and $\log g$ by comparison with synthetic spectra using the GSSP code. Due to binarity and poor resolution, the metallicity estimation is unreliable and cannot be compared to the cluster metallicity. To improve the SNR of the line profile, we applied the least-squares deconvolution (LSD) method (Donati et al. 1997). The LSD profile (Fig. 25) was used to calculate the $v \sin i$ and radial velocity of the star. The best-fitting results of our analysis are presented in Table 7.

9 SUMMARY

Our ground-based observations revealed 25 member variables and 85 field variables within a 9 arcmin radius field of NGC 2126. Our research was focused on member variables and stars with promising LCs in the *TESS* data. We discovered 18 new variable cluster members from the ground.

In *TESS*, we identified counterparts for 11 known variables, including 6 members and 5 field stars. Furthermore, we identified a new field star as a rotational variable based on *TESS* LC. *TESS* frequency spectra show distinctive pulsation peaks, especially for δ Scuti stars. These frequencies can be used to conduct asteroseismic studies on member pulsating stars. Aside from that, the cluster has a higher metallicity than the solar metallicity, implying the presence of chemically peculiar stars in the cluster. Thus, a spectroscopic investigation can benefit our understanding of the member variables.

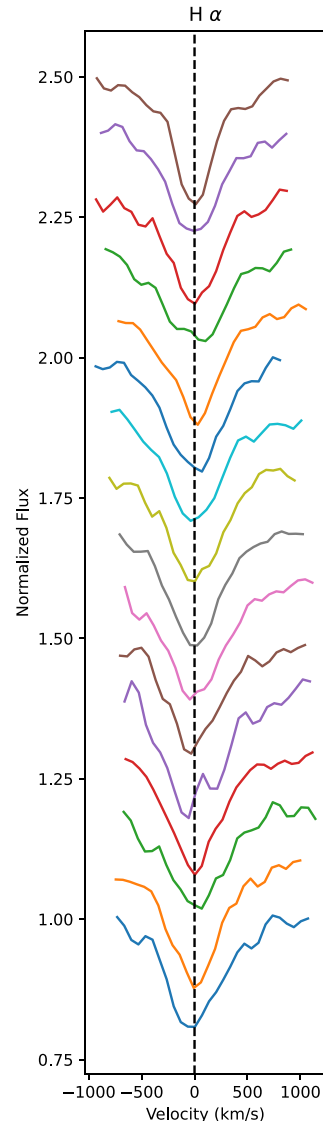


Figure 23. The $H\alpha$ line of low-resolution spectra at different phases obtained with HFOSC equipped on HCT. The normalized flux for each spectrum was added by 0.1 for visual clarity. The phase increases from 0 to 1 from bottom to top.

We attempted to solve the *TESS* contamination problem by using custom apertures for our sources and cross-matching detected frequencies to ground-based frequencies. This method was useful for stars that produced strong signals in *TESS*.

We used *TESS* data to model the EBs V4, V6, and ZV3 by combining their *TESS* LCs. However, this model still lacks the support of spectroscopic radial velocity measurements. Due to a lack of data, ZV3 had not previously been modelled or its orbital period determined. We utilized the continuous LCs from *TESS* data to model this star, thereby establishing the linear ephemeris and determining the orbital period.

The intrinsic variability and eclipses of the pulsating EB V551 Aur were modelled simultaneously to determine its parameters. This resulted in slightly different parameter estimates than those reported in previous literature. The low-resolution spectroscopy confirms the spectral line profile variation for this system, indicating that it is a

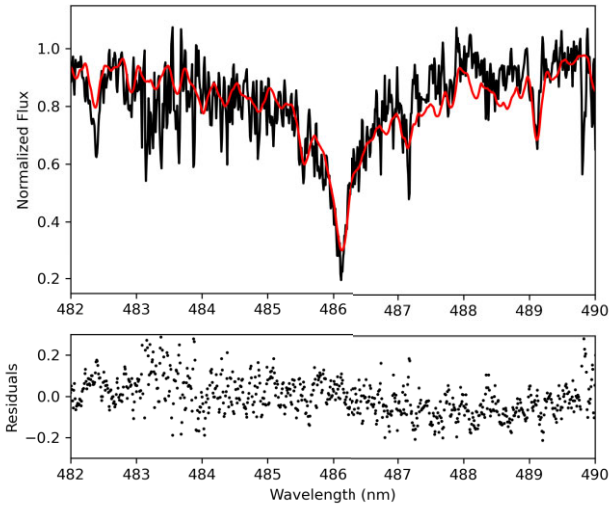


Figure 24. The top panel shows the $H\beta$ line (black) of the medium-resolution spectrum acquired for V551 Aur at an orbital phase 0.96 and the best-fitting synthetic spectrum (red). The bottom panel shows the residuals of the fit.

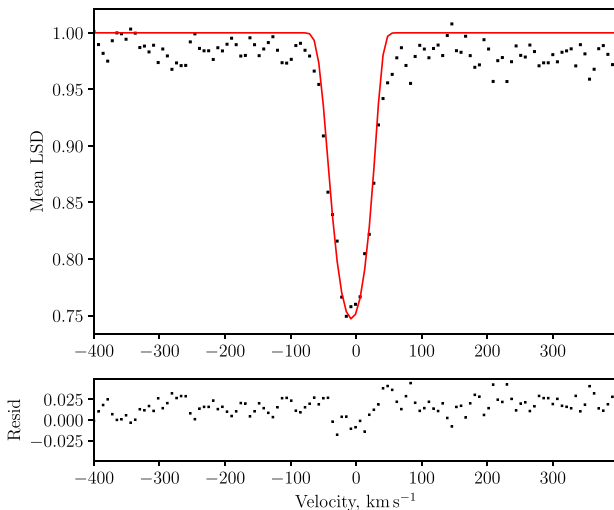


Figure 25. The top panel shows the mean LSD profile of the medium-resolution spectra (square marker) for V551 Aur. A rotationally broadened line profile (solid curve) was fit to these data to find $v \sin i$ and radial velocity. The bottom panel gives the residuals of the fit.

Table 7. The table shows the spectroscopic parameters that were found for V551 Aur using the medium-resolution spectrum. The parameters were found by fitting synthetic spectra to the $H\beta$ line and line profile fitting to the LSD profile.

Parameters	$H\beta$	LSD
T_{eff}	6458 ± 361 K	–
$\log g$	3.0 ± 1.49	–
RV	–	-8.4 ± 1.2 km s $^{-1}$
$v \sin i$	–	44.0 ± 2.5 km s $^{-1}$

spectroscopic binary. The medium-resolution spectra provided better estimates of spectroscopic parameters for V551 Aur.

10 CONCLUSIONS

This project was initiated to search and study pulsating variables in the open star cluster NGC 2126, utilizing ground-based observations, *Gaia* data, and *TESS* FFIs for improved analysis. This study led us to draw the following conclusions:

(i) Our study demonstrates that *TESS* LCs alone are unreliable in the case of open clusters due to contamination. To address this issue and fully utilize the *TESS* data, one must integrate *Gaia* data and ground-based observations. This allows us to identify contaminated sources and make better use of the frequency resolution provided by *TESS*.

(ii) V551 Aur, which was known to exhibit pulsations in one of its components, was found to be a spectroscopic binary with membership to the cluster. To understand this system and model it accurately, high-resolution spectroscopic follow-up observations covering this star’s orbital phase are required. Due to the star’s faintness, we intend to use observations with a larger aperture telescope.

From isochrone fitting, we determined $\log \text{age} \sim 9.2$, a metallicity ~ 0.016 , and a distance ~ 1.2 kpc for the cluster. Our results are in agreement with previous determinations from Chehlaeh et al. (2018), but with slight differences ($\log \text{age} \sim 9.1$, $Z \sim 0.019$, and $d \sim 1.4$ kpc in Chehlaeh et al. 2018), possibly due to the improved magnitude, colour, proper motion, and parallax from *Gaia*.

Our observations of NGC 2126 are limited to a few nights. More observations are required for a detailed frequency analysis of the detected targets. Therefore, we plan to conduct further observations for the cluster using the observing facilities at ARIES, Nainital.

ACKNOWLEDGEMENTS

We are grateful to the Indian and Belgian funding agencies Department of Science and Technology (DST) (DST/INT/Belg/P-09/2017) and Belgian Science Policy Office (BELSPO) (BL/33/IN12) for providing financial support to carry out this work. AD acknowledges the financial support received from Department of Science and Technology’s Innovation in Science Pursuit for Inspired Research (DST-INSPIRE) Fellowship Programme (No. DST/INSPIRE Fellowship/2020/IF200245).

DATA AVAILABILITY

The data underlying this article will be shared upon request to the corresponding author. The observations reported in this paper were obtained using the 1.04 m ST, 1.3 m DFOT and 3.6 m DOT telescopes at ARIES, Nainital, India, the 2 m HCT at IAO, Hanle, the High Altitude Station of Indian Institute of Astrophysics, Bangalore, India and 2.4 m telescope at Thai National Observatory (TNO), Chiang Mai, Thailand. This research has made use of the ‘Set of Identifications, Measurements and Bibliography for Astronomical Data’ (SIMBAD) database operated at CDS, Strasbourg, France. This work has made use of data from the European Space Agency (ESA) mission *Gaia* (<https://www.cosmos.esa.int/gaia>), processed by the *Gaia* Data Processing and Analysis Consortium (DPAC; <https://www.cosmos.esa.int/web/gaia/dpac/consortium>). Funding for the DPAC has been provided by national institutions, in particular the institutions participating in the *Gaia* Multilateral Agreement. This

paper includes data collected by the *TESS* mission, which are publicly available from the Mikulski Archive for Space Telescopes (MAST) at the Space Telescope Science Institute (STScI).

REFERENCES

- Aerts C., 2021, *Rev. Mod. Phys.*, 93, 015001
- Aerts C., Christensen-Dalsgaard J., Kurtz D. W., 2010, *Asteroseismology*. Springer, Berlin
- Ashoka B. N. et al., 2000, *Bull. Astron. Soc. India*, 28, 251
- Balona L. A., 2013, *MNRAS*, 431, 2240
- Bedding T. R. et al., 2023, *ApJ*, 946, L10
- Brasseur C. E., Phillip C., Fleming S. W., Mullally S. E., White R. L., 2019, *Astrophysics Source Code Library*, record ascl:1905.007
- Bressan A., Marigo P., Girardi L., Salasnich B., Dal Cero C., Rubele S., Nanni A., 2012, *MNRAS*, 427, 127
- Charbonneau P., 1995, *ApJS*, 101, 309
- Chehlaeh N., Mkrichian D., Lampens P., Konomjinda S., Kim S. L., Van Cauteren P., Kusakin A. V., Glazunova L., 2018, *MNRAS*, 480, 1850
- Chen Y., Girardi L., Bressan A., Marigo P., Barbieri M., Kong X., 2014, *MNRAS*, 444, 2525
- Chen Y., Bressan A., Girardi L., Marigo P., Kong X., Lanza A., 2015, *MNRAS*, 452, 1068
- Cowsik R., Srinivasan R., Prabhu T., 2002, in Vernin J., Benkhaldoun Z., Muñoz-Tuñón C., eds, *ASP Conf. Ser. Vol. 266, Astronomical Site Evaluation in the Visible and Radio Range*. Astron. Soc. Pac., San Francisco, p. 424
- Danielski C., Babusiaux C., Ruiz-Dern L., Sartoretti P., Arenou F., 2018, *A&A*, 614, A19
- Deb S., Singh H. P., 2009, *A&A*, 507, 1729
- Dileep A., Joshi S., Kurtz D. W., 2024, *Bull. Soc. R. Sci. Liege*, 93, 227
- Donati J. F., Semel M., Carter B. D., Rees D. E., Collier Cameron A., 1997, *MNRAS*, 291, 658
- Dupret M. A., Grigahcène A., Garrido R., Gabriel M., Scuflaire R., 2005, *A&A*, 435, 927
- Feinstein A. D. et al., 2019, *PASP*, 131, 094502
- Fonnesbeck C., Patil A., Huard D., Salvatier J., 2015, *Astrophysics Source Code Library*, record ascl:1506.005
- Foreman-Mackey D., 2018, *Res. Notes Am. Astron. Soc.*, 2, 31
- Foreman-Mackey D., Agol E., Ambikasaran S., Angus R., 2017, *AJ*, 154, 220
- Foreman-Mackey D. et al., 2021, *J. Open Source Softw.*, 6, 3285
- Gaia Collaboration, 2016, *A&A*, 595, A1
- Gaia Collaboration, 2023, *A&A*, 674, A1
- Gáspár A. et al., 2003, *A&A*, 410, 879
- Han T., Brandt T. D., 2023, *AJ*, 165, 71
- Handler G. et al., 2009, *ApJ*, 698, L56
- Joshi S. et al., 2003, *MNRAS*, 344, 431
- Joshi S., Mary D. L., Martinez P., Kurtz D. W., Girish V., Seetha S., Sagar R., Ashoka B. N., 2006, *A&A*, 455, 303
- Joshi S., Mary D. L., Chakradhari N. K., Tiwari S. K., Billaud C., 2009, *A&A*, 507, 1763
- Joshi S., Ryabchikova T., Kochukhov O., Sachkov M., Tiwari S. K., Chakradhari N. K., Piskunov N., 2010, *MNRAS*, 401, 1299
- Joshi S. et al., 2012, *MNRAS*, 424, 2002
- Joshi Y. C., Jagirdar R., Joshi S., 2016a, *Res. Astron. Astrophys.*, 16, 63
- Joshi S. et al., 2016b, *A&A*, 590, A116
- Joshi S., Semenkov E., Moiseeva A., Sharma K., Joshi Y. C., Sachkov M., Singh H. P., Yerra B. K., 2017, *MNRAS*, 467, 633
- Joshi Y. C., Maurya J., John A. A., Panchal A., Joshi S., Kumar B., 2020a, *MNRAS*, 492, 3602
- Joshi Y. C., John A. A., Maurya J., Panchal A., Kumar B., Joshi S., 2020b, *MNRAS*, 499, 618
- Joshi Y. C., Bangia T., Jaiswar M. K., Pant J., Reddy K., Yadav S., 2022a, *J. Astron. Instrum.*, 11, 2240004
- Joshi S. et al., 2022b, *MNRAS*, 510, 5854
- King I., 1962, *AJ*, 67, 471
- Kumar B. et al., 2018, *Bull. Soc. R. Sci. Liege*, 87, 29
- Lampens P., 2021, *Galaxies*, 9, 28
- Landolt A. U., 1992, *AJ*, 104, 340
- Lata S. et al., 2023, *MNRAS*, 520, 1092
- Lenz P., Breger M., 2004, in Ziznovsky J., Adelman S. J., Weiss W. W., eds, *Proc. IAU Symp. 224, The A-Star Puzzle*. Cambridge Univ. Press, Cambridge, p. 786
- Li G. et al., 2024, *A&A*, 686, A142
- Lightkurve Collaboration, 2018, *Astrophysics Source Code Library*, record ascl:1812.013
- Liu N., Zhang X.-B., Ren A.-B., Deng L.-C., Luo Z.-Q., 2012, *Res. Astron. Astrophys.*, 12, 671
- Luger R., Agol E., Foreman-Mackey D., Fleming D. P., Lustig-Yaeger J., Deitrick R., 2019, *AJ*, 157, 64
- Mamajek E. E., Hillenbrand L. A., 2008, *ApJ*, 687, 1264
- Martinez P. et al., 2001, *A&A*, 371, 1048
- Maurya J., Joshi Y. C., Panchal A., Gour A. S., 2023, *AJ*, 165, 90
- Montgomery M. H., O'Donoghue D., 1999, *Delta Scuti Star Newsl.*, 13, 28
- Murphy S. J., Zenodo Geneva, Switzerland 2019, *Pulsating Stars in Binary Systems: A Review*, <https://doi.org/10.5281/zenodo.2533474>
- Pamos Ortega D., Mirouh G. M., García Hernández A., Suárez Yanes J. C., Barceló Forteza S., 2023, *A&A*, 675, A167
- Pamyatnykh A. A., 2000, in Breger M., Montgomery M., eds, *ASP Conf. Ser. Vol. 210, Delta Scuti and Related Stars*. Astron. Soc. Pac., San Francisco, p. 215
- Panchal A., Joshi Y. C., De Cat P., Lampens P., Goswami A., Tiwari S. N., 2023, *MNRAS*, 521, 677
- Pandey S. B., Yadav R. K. S., Nanjappa N., Yadav S., Reddy B. K., Sahu S., Srinivasan R., 2018, *Bull. Soc. R. Sci. Liege*, 87, 42
- Perren G. I., Vázquez R. A., Piatti A. E., 2015, *A&A*, 576, A6
- Pigulski A., 2006, in Aerts C., Sterken C., eds, *ASP Conf. Ser. Vol. 349, Astrophysics of Variable Stars*. Astron. Soc. Pac., San Francisco, p. 137
- Poznanski D., Prochaska J. X., Bloom J. S., 2012, *MNRAS*, 426, 1465
- Prša A., Zwitter T., 2005, *ApJ*, 628, 426
- Ricker G. R., 2014, *J. Am. Assoc. Var. Star Obs.*, 42, 234
- Sarkar M. et al. 534 3211–3220, 2024, *MNRAS*
- Stetson P. B., 1987, *PASP*, 99, 191
- Stetson P. B., 1992, in Worrall D. M., Biemesderfer C., Barnes J., eds, *ASP Conf. Ser. Vol. 25, Astronomical Data Analysis Software and Systems I*. Astronomical Society of the Pacific, San Francisco, 297
- Tang J., Bressan A., Rosenfield P., Slemmer A., Marigo P., Girardi L., Bianchi L., 2014, *MNRAS*, 445, 4287
- Tkachenko A., 2015, *A&A*, 581, A129
- Torres G., 2010, *AJ*, 140, 1158
- Trust O., Jurua E., De Cat P., Joshi S., Lampens P., 2021, *MNRAS*, 504, 5528
- Trust O., Mashonkina L., Jurua E., De Cat P., Tsymbal V., Joshi S., 2023, *MNRAS*, 524, 1044
- Wilson R. E., 1994, *PASP*, 106, 921
- Wu Z. Y., Tian K. P., Balaguer-Núñez L., Jordi C., Zhao L., Guibert J., 2002, *A&A*, 381, 464
- Yadav R. K. S. et al., 2022, *J. Astron. Instrum.*, 11, 2240006
- Zhang X. B., Deng L. C., Luo C. Q., 2012, *AJ*, 144, 141
- Zong W., Charpinet S., Vauclair G., Giammichele N., Van Grootel V., 2016, *A&A*, 585, A22

APPENDIX A: FIELD STARS

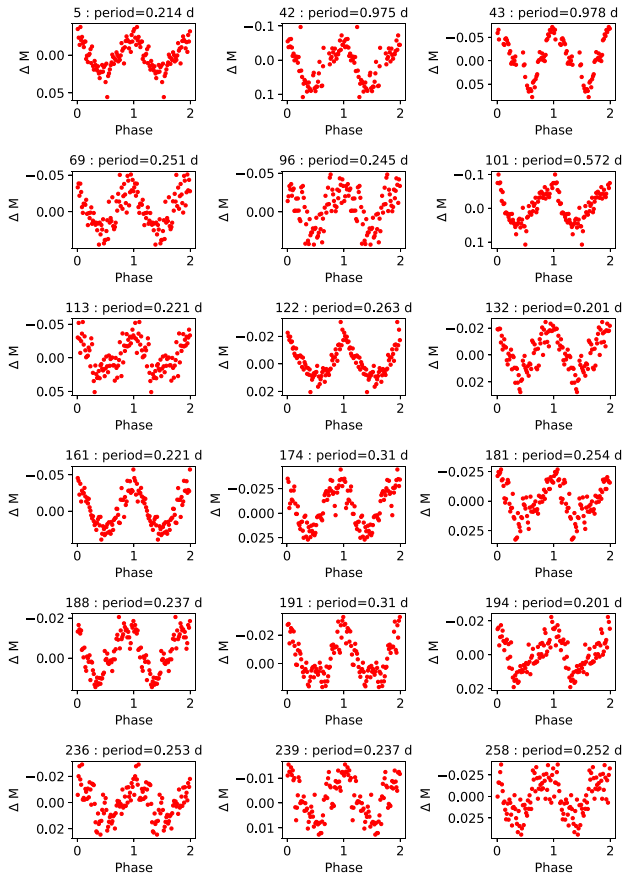


Figure A1. The phased V-band LCs of newly detected field variables in NGC 2126. Their respective IDs and periods are given as the title of each figure.

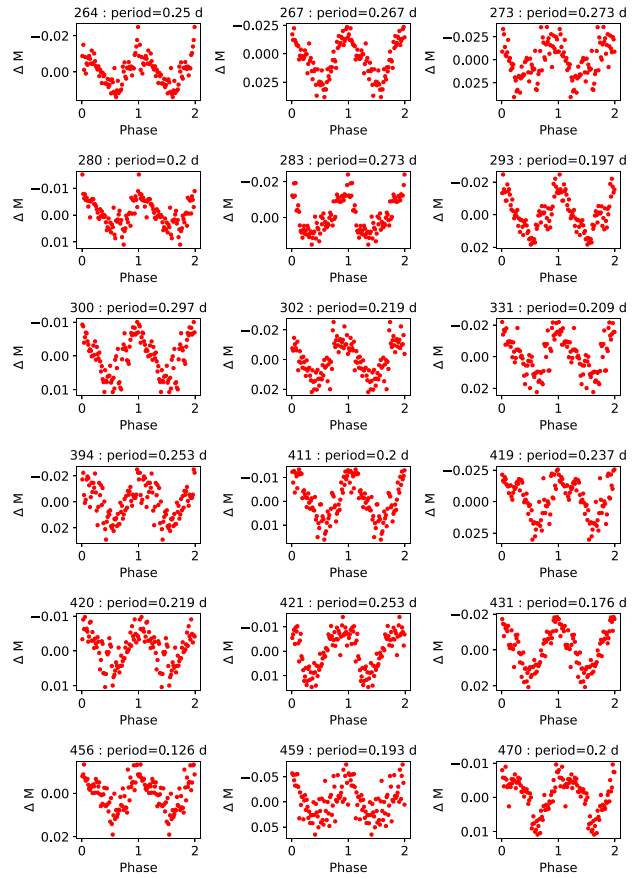


Figure A2. New variables – continued.

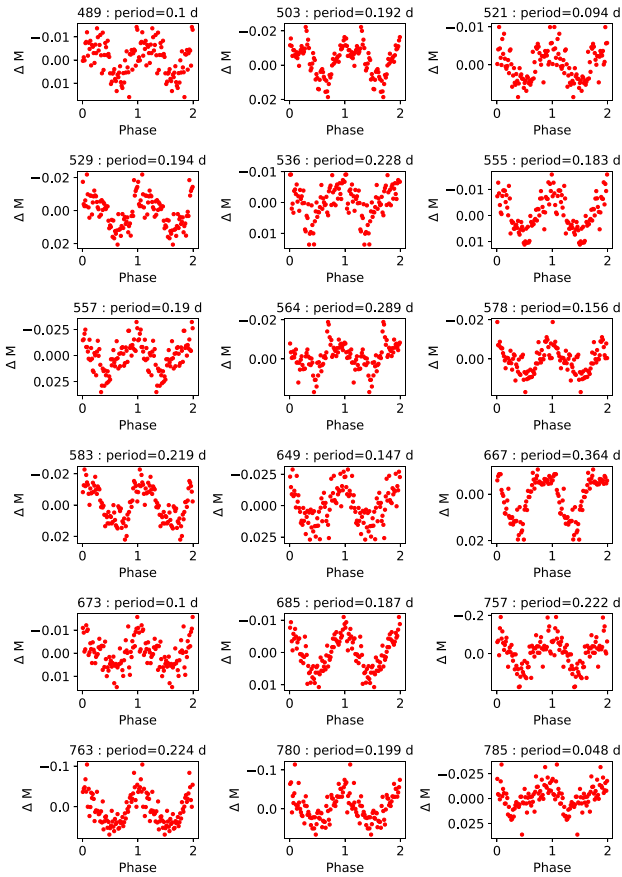


Figure A3. New variables – continued.

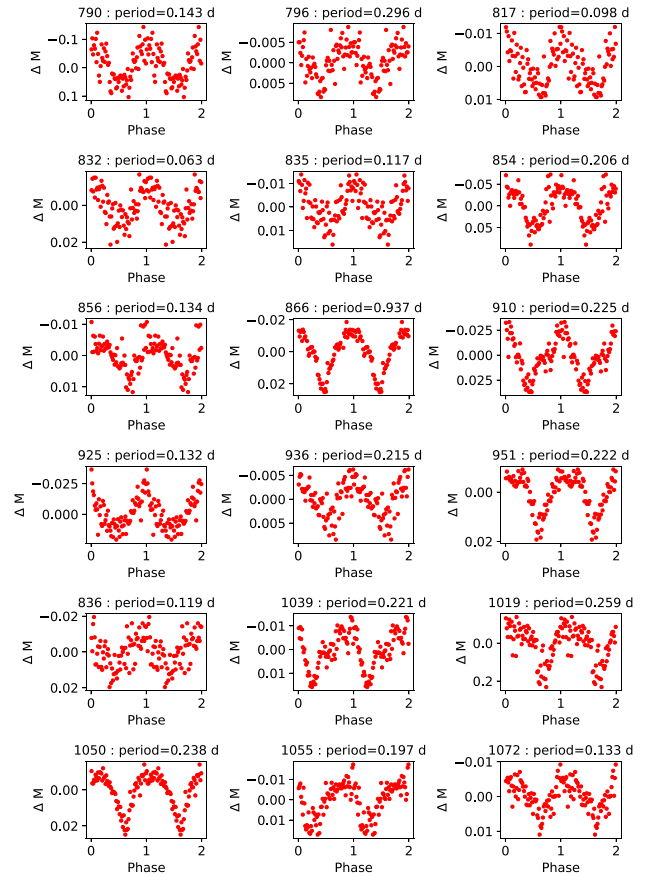


Figure A4. New variables – continued.

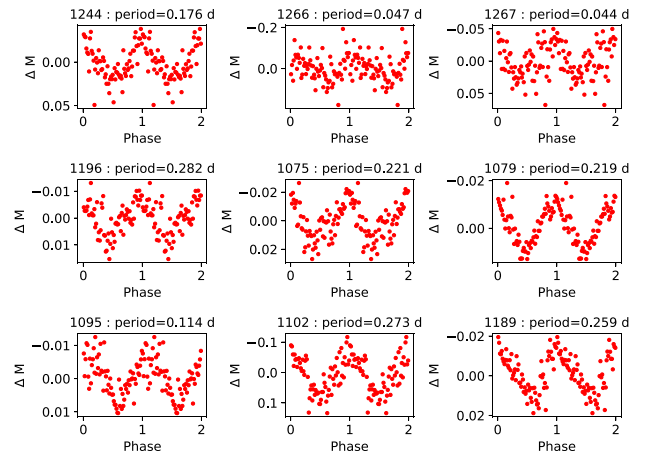


Figure A5. New variables – continued.

Table A1. The newly detected field variables from ground observations are listed with their ID, corrected magnitude, dominant frequency detected, and their corresponding amplitudes.

ID	RA	Dec.	Mag (mag)	Frequency (d ⁻¹)	Amp (mag)	ID	RA	Dec.	Mag (mag)	Frequency (d ⁻¹)	Amp (mag)
5	90.693 528	49.732 833	17.272	2.340	0.027	536	90.857 778	49.880 417	16.201	2.197	0.010
42	90.818 583	49.742 389	18.303	0.513	0.073	555	90.452 556	49.881 361	15.840	2.734	0.011
43	90.720 028	49.742 278	17.485	0.511	0.063	557	90.442 917	49.881 528	17.627	2.634	0.020
69	90.807 361	49.751 944	18.122	1.992	0.062	564	90.689 056	49.884 472	13.588	1.729	0.011
96	90.649 444	49.760 167	18.465	2.042	0.036	578	90.490 917	49.884 139	16.378	3.197	0.010
101	90.792 972	49.763 167	18.083	0.874	0.075	583	90.712 944	49.886 389	15.941	0.219	0.013
113	90.806 667	49.766 194	18.301	2.265	0.033	649	90.758 222	49.895 194	17.827	3.391	0.030
122	90.430 194	49.766 194	14.958	1.898	0.022	667	90.747 583	49.896 778	15.418	1.374	0.013
132	90.841 667	49.771 611	16.458	2.487	0.018	673	90.831 528	49.897 778	16.188	4.981	0.012
161	90.663 667	49.781 611	17.450	2.258	0.038	685	90.529 556	49.897 194	15.457	2.677	0.008
174	90.683 972	49.786 639	16.978	1.615	0.034	763	90.857 111	49.911 806	18.298	2.228	0.120
181	90.815 611	49.789 611	16.520	1.972	0.024	780	90.870 333	49.913 639	18.924	2.508	0.048
188	90.691 639	49.793 500	14.827	2.112	0.018	785	90.445 639	49.911 389	17.480	10.318	0.020
191	90.770 583	49.794 667	16.312	1.615	0.031	790	90.626 972	49.913 194	19.299	3.500	0.073
194	90.868 000	49.795 333	15.880	2.487	0.018	796	90.487 861	49.912 889	15.630	1.690	0.006
236	90.814 278	49.806 944	16.793	1.978	0.016	817	90.450 556	49.915 833	16.551	5.111	0.008
239	90.580 361	49.805 833	15.727	2.112	0.011	832	90.689 083	49.920 194	16.610	7.970	0.015
258	90.855 111	49.812 944	18.185	1.985	0.050	835	90.456 444	49.918 833	16.667	4.260	0.012
264	90.769 750	49.813 583	15.541	1.996	0.011	854	90.704 528	49.925 222	17.714	2.424	0.052
267	90.624 278	49.813 194	16.557	1.875	0.030	856	90.469 889	49.923 417	15.634	3.722	0.010
273	90.665 056	49.814 778	18.306	1.832	0.030	866	90.495 306	49.926 917	14.498	0.533	0.019
280	90.606 861	49.816 028	14.400	2.496	0.007	910	90.795 611	49.939 806	16.296	2.225	0.029
283	90.738 278	49.816 972	15.930	1.830	0.017	925	90.532 194	49.941 667	17.325	3.780	0.020
293	90.554 944	49.819 472	16.688	2.533	0.017	936	90.445 556	49.944 222	14.031	0.215	0.005
300	90.638 722	49.821 000	14.776	1.685	0.009	951	90.835 222	49.951 389	14.348	2.251	0.012
302	90.700 750	49.822 222	16.736	2.287	0.020	836	90.466 111	49.919 111	17.283	4.217	0.015
331	90.569 389	49.829 278	16.639	2.390	0.016	1039	90.521 861	49.974 750	15.712	2.263	0.018
394	90.775 917	49.849 889	17.145	1.973	0.017	1019	90.484 417	49.969 278	19.470	1.932	0.126
411	90.622 750	49.853 278	15.926	2.502	0.013	1050	90.847 750	49.978 333	13.020	2.104	0.014
419	90.515 722	49.854 000	16.923	2.112	0.025	1055	90.858 417	49.980 889	16.489	2.538	0.019
420	90.546 167	49.854 917	14.862	2.281	0.007	1072	90.555 861	49.983 944	15.467	3.764	0.007
421	90.842 778	49.857 056	15.732	1.973	0.011	1244	90.781 139	50.027 389	17.733	2.843	0.033
431	90.828 194	49.858 472	15.247	2.840	0.018	1266	90.614 139	50.031 250	19.602	10.637	0.054
456	90.637 583	49.862 139	16.486	3.967	0.011	1267	90.747 306	50.032 417	18.748	11.270	0.035
459	90.705 750	49.863 694	18.543	2.588	0.040	1196	90.541 778	50.012 444	14.887	1.775	0.017
470	90.518 778	49.864 222	14.798	2.500	0.007	1075	90.873 500	49.987 528	17.240	2.263	0.019
489	90.530 833	49.868 667	16.649	5.008	0.008	1079	90.830 778	49.988 194	13.016	2.287	0.015
503	90.469 333	49.871 417	15.547	2.608	0.016	1095	90.619 694	49.991 056	16.197	4.403	0.010
521	90.653 472	49.876 083	15.578	5.306	0.005	1102	90.526 806	49.991 806	18.745	1.829	0.083
529	90.475 611	49.875 667	16.745	2.573	0.015	1189	90.456 472	50.010 611	16.340	1.931	0.015

APPENDIX B: COLOUR-COLOUR DIAGRAM

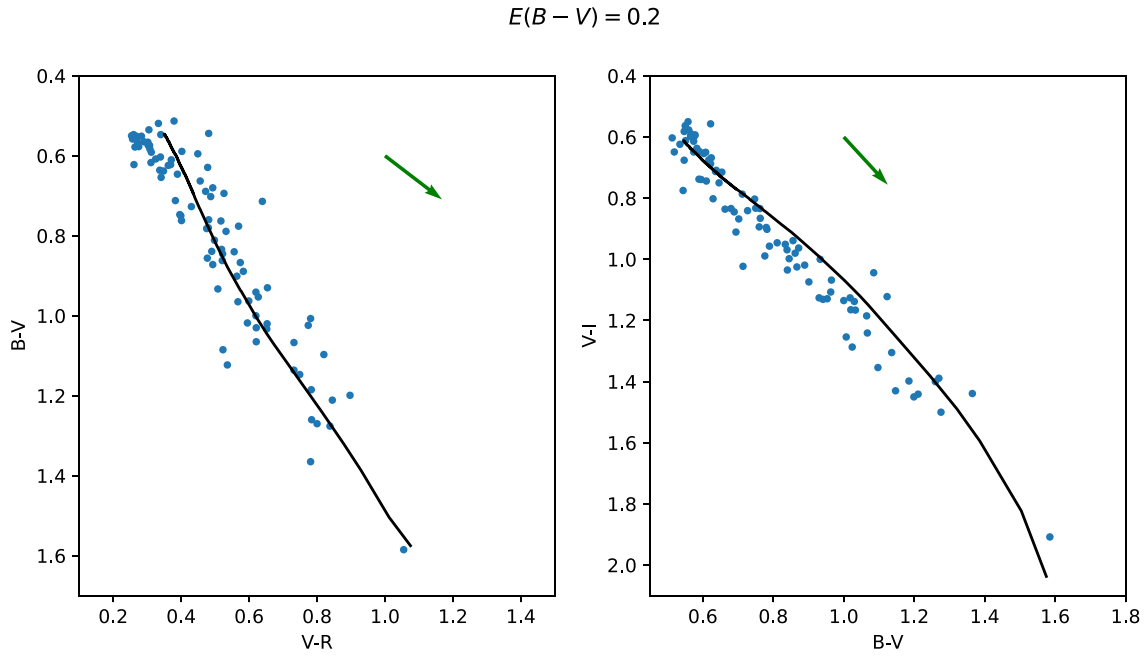


Figure B1. Left panel: The color index between V-band and R-band (V-R) versus B-V diagram for NGC 2126 member stars. Right panel: The B-V versus color index between V-band and I-band (V-I) diagram for NGC 2126 member stars. The solid lines in the plot are the theoretical isochrones and the arrow represents the reddening vector.

APPENDIX C: *TESS* PHOTOMETRY

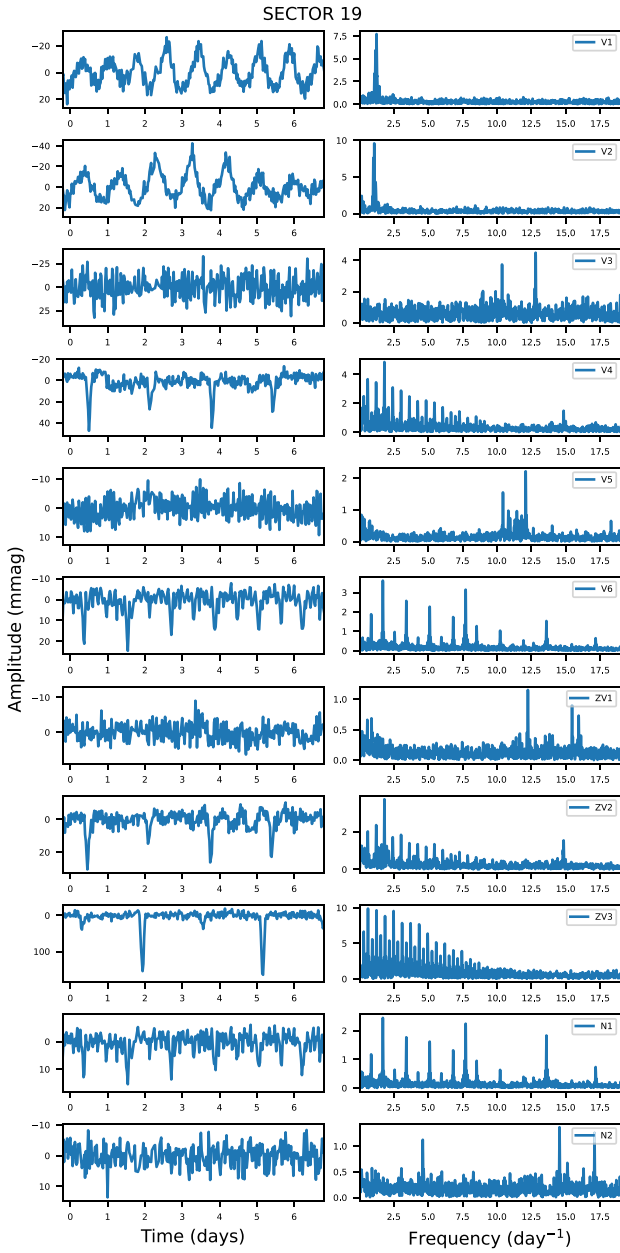


Figure C1. The Sector 19 LCs and the corresponding frequency spectra of known variables in NGC 2126.

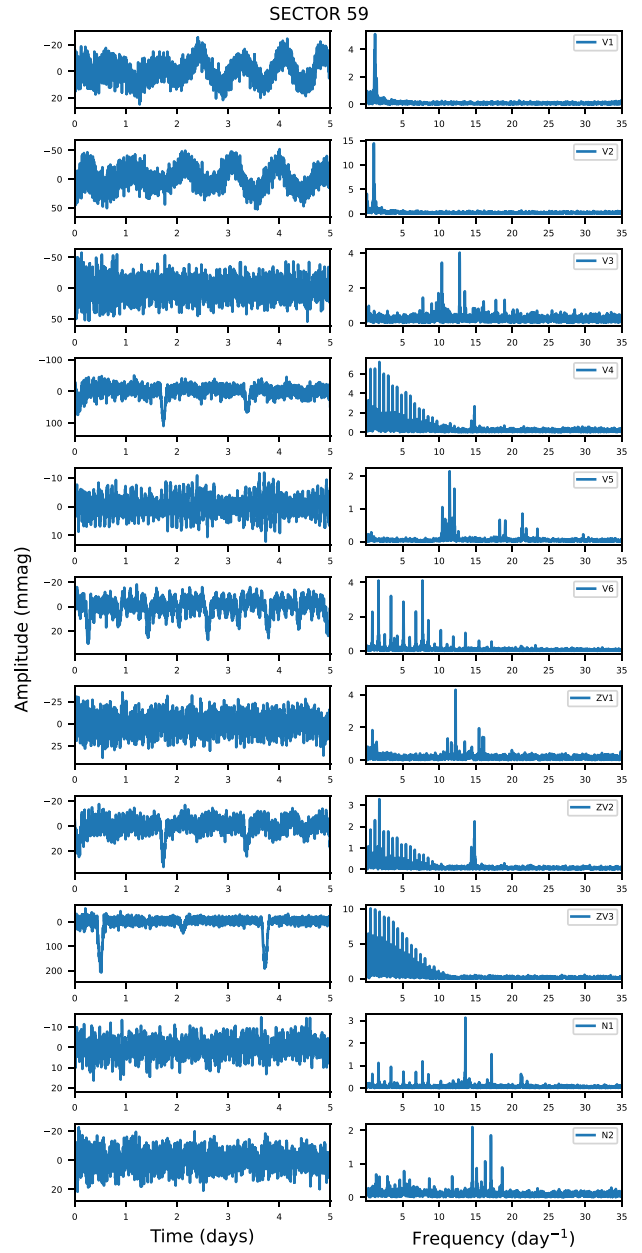


Figure C2. The Sector 59 LCs and the corresponding frequency spectra of known variables in NGC 2126.

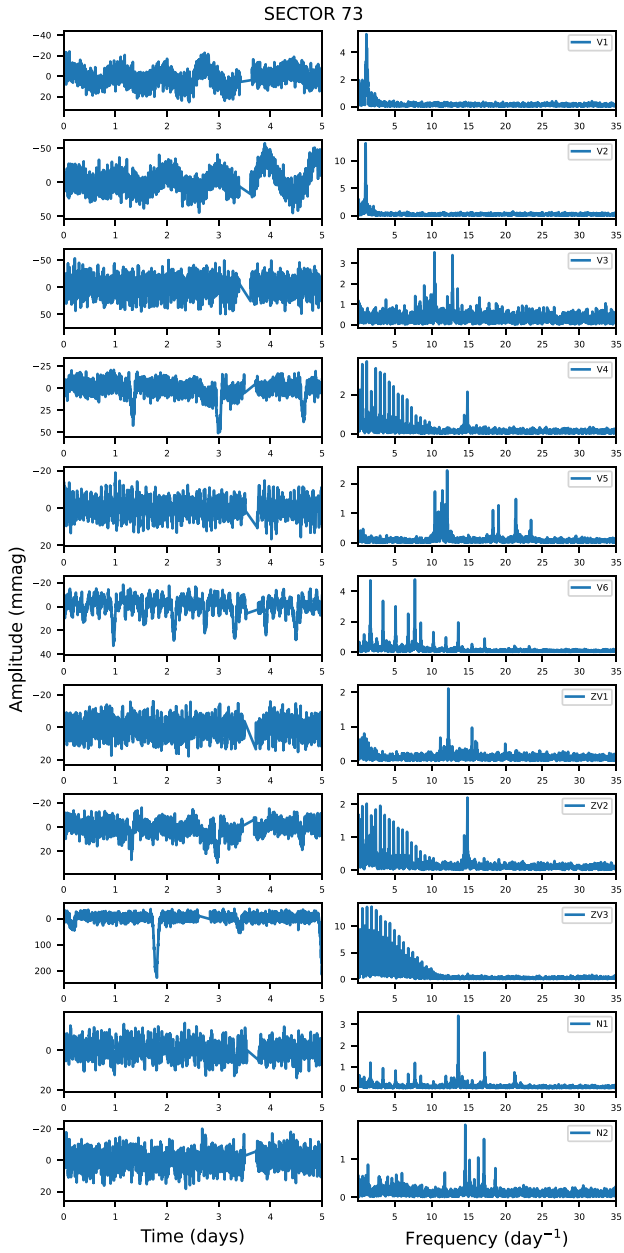


Figure C3. The Sector 73 LCs and the corresponding frequency spectra of known variables in NGC 2126.

Table C1. List of detected pulsational frequencies for Sectors 19, 59, and 73 for the stars without contamination. Their respective frequencies, amplitudes, and SNR are listed. The significance criterion was based on the minimum SNR of 5.6 and above.

ID	Sector	Frequency ID	Frequency (d^{-1})	Amplitude (mmag)	SNR		
V1	19	$f_{V1,19,1}$	1.2475 ± 0.0008	7.8 ± 0.3	11.1		
		$f_{V1,19,2}$	1.156 ± 0.001	4.5 ± 0.3	6.4		
		$f_{V1,59,1}$	1.2355 ± 0.0003	5.53 ± 0.08	19.2		
	59	$f_{V1,59,2}$	1.1597 ± 0.0003	5.37 ± 0.08	17.9		
		$f_{V1,59,3}$	1.1804 ± 0.0004	4.01 ± 0.08	13.6		
		$f_{V1,59,4}$	1.2893 ± 0.0008	2.00 ± 0.08	7.0		
		$f_{V1,59,5}$	1.4460 ± 0.0009	1.68 ± 0.08	6.1		
		73	$f_{V1,73,1}$	1.1485 ± 0.0004	5.7 ± 0.1	9.8	
			$f_{V1,73,2}$	1.2362 ± 0.0005	4.7 ± 0.1	8.9	
			$f_{V1,73,3}$	1.1136 ± 0.0008	3.0 ± 0.1	5.1	
		V2	19	$f_{V2,19,1}$	1.0771 ± 0.0007	8.3 ± 0.3	13.9
				$f_{V2,19,2}$	1.013 ± 0.001	5.7 ± 0.3	9.9
$f_{V2,19,3}$	1.176 ± 0.001			5.1 ± 0.3	9.3		
59	$f_{V2,59,1}$		1.0645 ± 0.0002	14.3 ± 0.2	25.9		
	$f_{V2,59,2}$		1.1768 ± 0.0007	5.2 ± 0.2	8.9		
	$f_{V2,59,3}$		1.019 ± 0.001	3.6 ± 0.2	6.1		
73	$f_{V2,73,1}$		1.0652 ± 0.0003	14.0 ± 0.2	18.9		
	$f_{V2,73,2}$		1.1724 ± 0.0008	5.1 ± 0.2	7.3		
V3	19		$f_{V3,19,1}$	12.816 ± 0.003	4.5 ± 0.5	8.1	
			$f_{V3,19,2}$	10.372 ± 0.003	3.7 ± 0.5	5.5	
	59		$f_{V3,59,1}$	12.814 ± 0.001	4.0 ± 0.2	16.2	
			$f_{V3,59,2}$	10.374 ± 0.001	3.4 ± 0.2	8.3	
	73	$f_{V3,73,1}$	13.514 ± 0.002	1.8 ± 0.2	6.7		
		$f_{V3,73,2}$	10.374 ± 0.002	3.6 ± 0.3	7.8		
V5	19	$f_{V5,19,1}$	12.091 ± 0.001	2.2 ± 0.1	10.4		
		$f_{V5,19,2}$	10.440 ± 0.002	1.6 ± 0.1	7.5		
		59	$f_{V5,59,1}$	11.4365 ± 0.0003	2.24 ± 0.03	34.2	
			$f_{V5,59,2}$	12.0923 ± 0.0004	1.63 ± 0.03	27.3	
			$f_{V5,59,3}$	10.4384 ± 0.0006	1.06 ± 0.03	23.5	
			$f_{V5,59,4}$	21.4049 ± 0.0007	0.84 ± 0.03	15.1	
			$f_{V5,59,5}$	11.8053 ± 0.0008	0.76 ± 0.03	12.2	
			$f_{V5,59,6}$	10.8224 ± 0.0009	0.70 ± 0.03	12.9	
			$f_{V5,59,7}$	18.2956 ± 0.0009	0.67 ± 0.03	12.5	
			$f_{V5,59,8}$	19.0526 ± 0.0009	0.64 ± 0.03	13.3	
			$f_{V5,59,9}$	11.3121 ± 0.0009	0.64 ± 0.03	9.7	
			$f_{V5,59,10}$	10.957 ± 0.001	0.42 ± 0.03	7.2	
	$f_{V5,59,11}$	23.452 ± 0.001	0.41 ± 0.03	9.6			
	$f_{V5,59,12}$	21.906 ± 0.002	0.38 ± 0.03	6.5			
	73	$f_{V5,59,13}$	12.639 ± 0.002	0.34 ± 0.03	6.5		
		$f_{V5,59,14}$	21.325 ± 0.002	0.33 ± 0.03	6.0		
		$f_{V5,73,1}$	12.0915 ± 0.0005	2.54 ± 0.06	24.0		
		$f_{V5,73,2}$	11.4449 ± 0.0006	1.79 ± 0.06	18.9		
		$f_{V5,73,3}$	10.4380 ± 0.0007	1.66 ± 0.06	19.1		
		$f_{V5,73,4}$	21.4070 ± 0.0008	1.47 ± 0.06	12.4		
		$f_{V5,73,5}$	11.8051 ± 0.0009	1.29 ± 0.06	12.3		
		$f_{V5,73,6}$	19.0531 ± 0.0009	1.30 ± 0.06	18.3		
		$f_{V5,73,7}$	18.298 ± 0.001	1.16 ± 0.06	13.5		
		$f_{V5,73,8}$	11.314 ± 0.001	1.17 ± 0.06	12.9		
$f_{V5,73,9}$		10.824 ± 0.001	1.13 ± 0.06	12.7			
$f_{V5,73,10}$		10.953 ± 0.001	0.92 ± 0.06	10.3			
ZV1	19	$f_{ZV1,19,1}$	12.253 ± 0.002	1.2 ± 0.1	9.2		
		$f_{ZV1,19,2}$	15.461 ± 0.003	0.9 ± 0.1	6.8		
	59	$f_{ZV1,59,1}$	12.2504 ± 0.0006	4.3 ± 0.1	21.9		
		$f_{ZV1,59,2}$	15.458 ± 0.001	2.0 ± 0.1	12.6		
		$f_{ZV1,59,3}$	16.120 ± 0.002	1.4 ± 0.1	9.4		
		$f_{ZV1,59,4}$	11.165 ± 0.002	1.4 ± 0.1	7.9		
		$f_{ZV1,59,5}$	15.943 ± 0.002	1.4 ± 0.1	9.5		
		$f_{ZV1,59,6}$	13.512 ± 0.002	1.3 ± 0.1	6.1		

Table C1 – continued

ID	Sector	Frequency ID	Frequency (d^{-1})		Amplitude (mmag)	SNR	
N2	73	$f_{ZV1,59,7}$	11.660 ± 0.003		1.1 ± 0.1	5.8	
		$f_{ZV1,73,1}$	12.2531 ± 0.0008	*	2.11 ± 0.08	16.0	
		$f_{ZV1,73,2}$	15.461 ± 0.002	*	0.97 ± 0.08	6.8	
	19	$f_{ZV1,73,3}$	11.171 ± 0.003		0.65 ± 0.08	5.2	
		$f_{N2,19,1}$	14.552 ± 0.002		1.4 ± 0.1	7.3	
		$f_{N2,19,2}$	17.094 ± 0.003		1.3 ± 0.1	7.8	
		$f_{N2,19,3}$	4.608 ± 0.003		1.1 ± 0.1	6.1	
		59	$f_{N2,59,1}$	14.5554 ± 0.0007	*	2.09 ± 0.07	22.7
			$f_{N2,59,2}$	17.0921 ± 0.0008		1.89 ± 0.07	21.1
			$f_{N2,59,3}$	16.304 ± 0.001		1.10 ± 0.07	13.6
			$f_{N2,59,4}$	18.627 ± 0.002		0.89 ± 0.07	10.0
			$f_{N2,59,5}$	15.134 ± 0.002		0.82 ± 0.07	9.5
			$f_{N2,59,6}$	5.206 ± 0.002		0.79 ± 0.07	5.7
			$f_{N2,59,7}$	$11.785 \pm 0.003^*$		0.61 ± 0.07	6.1
			$f_{N2,59,8}$	15.098 ± 0.003		0.57 ± 0.07	6.6
			$f_{N2,59,9}$	15.774 ± 0.003		0.49 ± 0.07	5.9
			73	$f_{N2,73,1}$	14.554 ± 0.001	*	1.89 ± 0.09
		$f_{N2,73,2}$		17.088 ± 0.001	*	1.55 ± 0.09	17.0
		$f_{N2,73,3}$		16.301 ± 0.002		1.08 ± 0.09	9.9
$f_{N2,73,4}$	15.138 ± 0.002			0.91 ± 0.09	6.8		
839	19	$f_{839,19,1}$	1.3530 ± 0.0006		21.6 ± 0.6	15.0	
		$f_{839,19,2}$	2.715 ± 0.003		4.5 ± 0.6	5.2	

Note. *Frequency values consistent with Chehlaeh et al. (2018).

Table C2. List of detected pulsational frequencies for Sectors 19, 59, and 73 for the stars that are contaminated. Their respective frequencies, amplitudes, and SNR are listed. The significance criterion was based on the minimum SNR of 5.6 and above.

ID	Sector	Frequency ID	Frequency (d^{-1})		Amplitude (mmag)	SNR		
V6	19	$f_{V6,19,1}$	7.7248 ± 0.0005	*	3.08 ± 0.07	46.8		
		$f_{V6,59,1}$	7.7266 ± 0.0004	*	4.10 ± 0.07	41.5		
	59	$f_{V6,59,1/2}$	3.862 ± 0.002		0.75 ± 0.07	8.2		
		$2f_{V6,59,1}$	15.450 ± 0.002	*	0.63 ± 0.07	7.9		
		73	$f_{V6,73,1}$	7.7270 ± 0.0002	*	4.77 ± 0.06	49.3	
			$f_{V6,73,1/2}$	3.864 ± 0.002		0.74 ± 0.06	7.8	
			$2f_{V6,73,1}$	15.454 ± 0.002	*	0.56 ± 0.06	8.8	
		ZV2	19	$f_{ZV2,19,1}$	14.851 ± 0.002	*	1.6 ± 0.2	7.7
				$f_{ZV2,59,1}$	14.852 ± 0.001	*	2.4 ± 0.2	14.2
59	$f_{ZV2,59,2}$		14.802 ± 0.003		1.3 ± 0.2	7.9		
	$f_{ZV2,59,3}$		14.409 ± 0.003		1.0 ± 0.2	6.8		
	$f_{ZV2,59,4}$		0.318 ± 0.002		1.2 ± 0.1	5.8		
	$f_{ZV2,59,5}$		1.815 ± 0.002	**	1.1 ± 0.1	5.7		
	73		$f_{ZV2,73,1}$	14.8394 ± 0.0008	*	2.53 ± 0.09	26.1	
$f_{ZV2,73,2}$			14.405 ± 0.002		1.01 ± 0.09	10.3		
$f_{ZV2,73,3}$			14.793 ± 0.002		1.07 ± 0.09	11.0		
N1			19	$f_{N1,19,1}$	13.5991 ± 0.0008	*	1.81 ± 0.07	19.4
	$f_{N1,19,2}$			17.176 ± 0.003	*	0.76 ± 0.07	10.4	
	59	$f_{N1,59,1}$	13.5969 ± 0.0009	*	1.70 ± 0.07	19.7		
		$f_{N1,59,2}$	17.177 ± 0.002	*	0.74 ± 0.07	8.4		
	73	$f_{N1,73,1}$	13.5972 ± 0.0003	*	3.38 ± 0.05	28.4		
		$f_{N1,73,2}$	17.1767 ± 0.0006	*	1.67 ± 0.05	24.6		
		$f_{N1,73,3}$	21.203 ± 0.001	*	0.71 ± 0.05	9.1		
		$f_{N1,73,4}$	21.348 ± 0.002		0.59 ± 0.05	7.8		

Notes. *Frequency values consistent with Chehlaeh et al. (2018).

**Frequency values consistent with Zhang et al. (2012).

APPENDIX D: BINARY EPHEMERIS

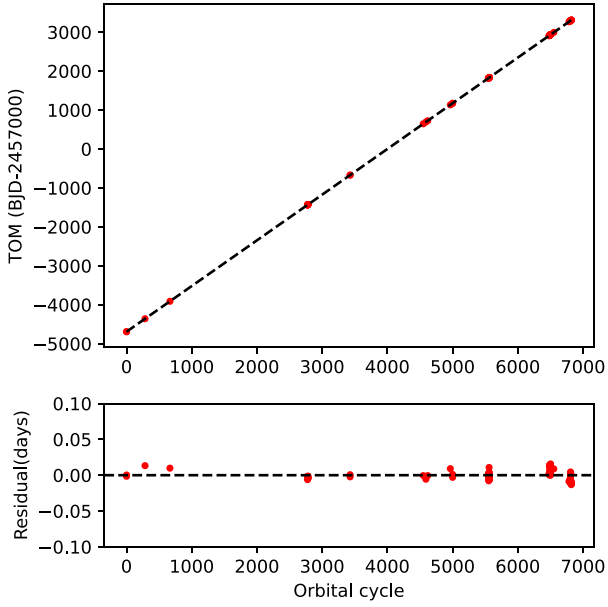


Figure D1. The top panel shows the linear ephemeris of V551 Aur by fitting a straight line to the observed TOM from all the *TESS* sectors along with the ground-based minima detected in this study and listed in Chehlaeh et al. (2018). The bottom panel shows the residuals of the fit.

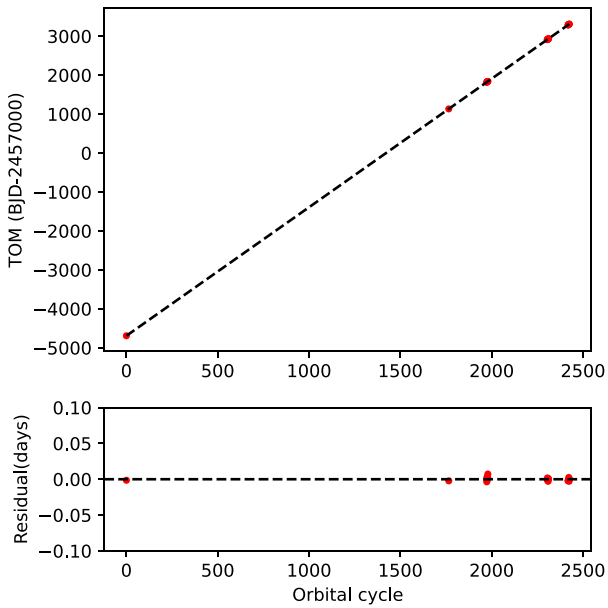


Figure D2. The top panel shows the linear ephemeris of V549 Aur by fitting a straight line to the observed TOM from all the *TESS* sectors and two eclipse minima given in Chehlaeh et al. (2018). The bottom panel shows the residuals of the fit.

APPENDIX E: EB MODELLING

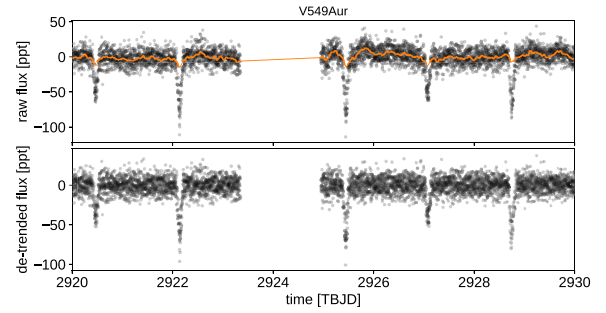


Figure E1. The top panel shows the Gaussian process model of V549 Aur. The bottom panel shows the residuals after subtracting the model.

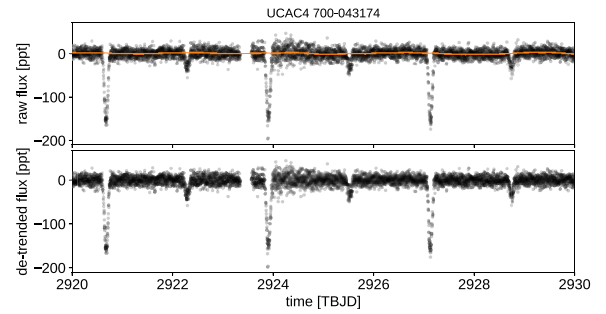


Figure E2. The top panel shows the Gaussian process model of V549 Aur. The bottom panel shows the residuals after subtracting the model.

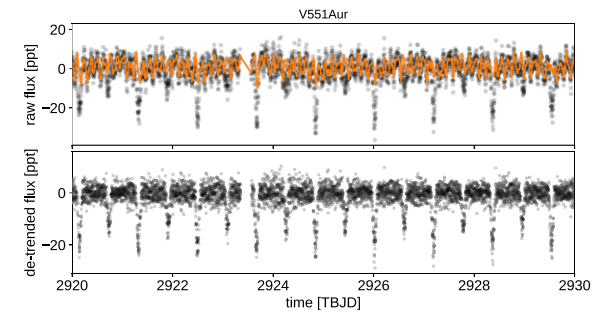


Figure E3. The top panel shows the Gaussian process model of V551 Aur for the pulsational variability. The bottom panel shows the residual LC after subtracting the pulsation model.

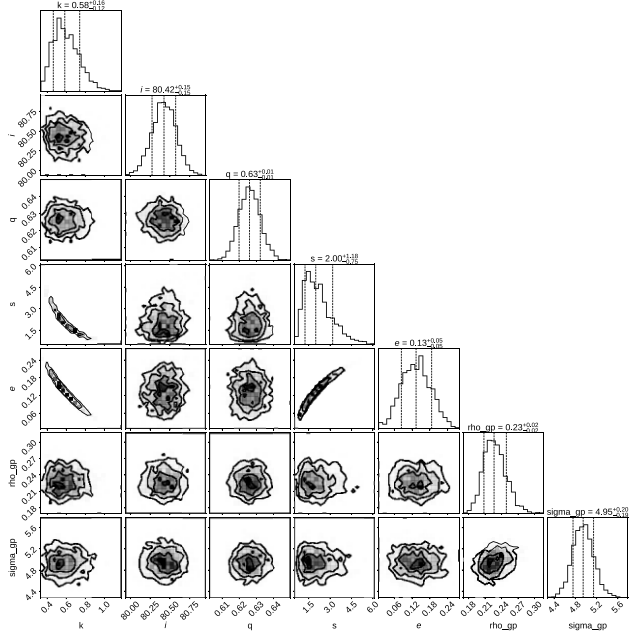


Figure E4. The figure shows the posterior distribution for the eclipse model and Gaussian process model from EXOPLANET code for V549 Aur.

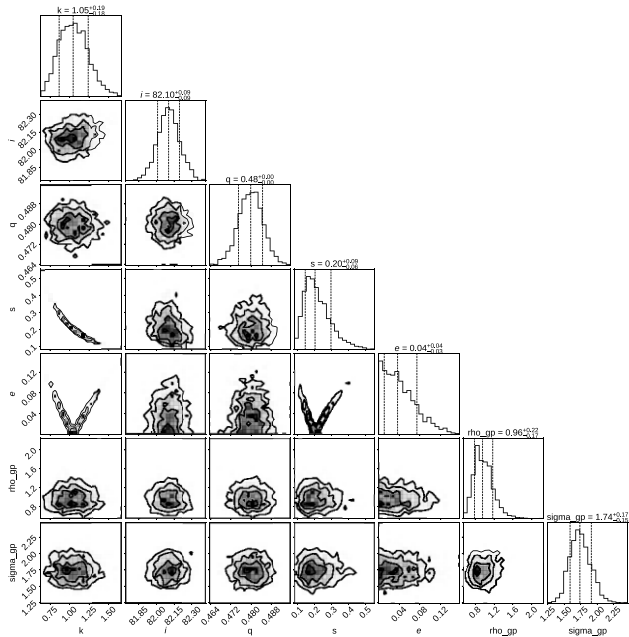


Figure E5. The figure shows the posterior distribution for the eclipse model and the Gaussian process model from EXOPLANET code for ZV3.

Table E1. The table gives the adopted prior distributions for the PYMC3 runs with 6000 samples. Here, $M1$ is the mass of the primary star, $R1$ is the radius of the primary star, k is the radius ratio, q is the mass ratio, s is the surface brightness ratio, and ecs represents the two orthogonal components of eccentricity ($e \cos \omega$ and $e \sin \omega$).

Parameters	V6	V4	ZV3
$\log(M1)$	Normal(log(1.375), 1.0)	Normal(log(1.05), 1.0)	Normal(log(1.20), 1.0)
$\log(R1)$	Normal(log(1.728), 1.0)	Normal(log(0.83), 1.0)	Normal(log(1.039), 1.0)
$\log(k)$	Normal(0.0, 10.0)	Normal(0.0, 10.0)	Normal(0.0, 10.0)
$\log(q)$	Normal(log(0.769), 0.01)	Normal(log(0.626), 0.01)	Normal(log(0.48), 0.01)
$\log(s)$	Normal(log(0.5), 10.0)	Normal(log(0.5), 10.0)	Normal(log(0.5), 10.0)
ecs	UnitDisk([1e-5, 0.0])	UnitDisk([1e-5, 0.0])	UnitDisk([1e-5, 0.0])

APPENDIX F: LOW-RESOLUTION SPECTROSCOPY

Table F1. The table lists the effective temperature (T_{eff}) and surface gravity ($\log g$) using *Gaia* DR3 gspot and the series of low-resolution spectra. The values of T_{eff} and $\log g$ were derived by fitting the observed spectra with synthetic spectra. The last row gives the mean T_{eff} and $\log g$ values of those derived from the individual spectra.

Source	T_{eff}	$\log g$
<i>Gaia</i> DR3 (gsphot)	5943	4.0
Low-resolution spectrum (this study)		
2021-08-15	5853 ± 213	3 ± 1
2021-09-13	5898 ± 178	4 ± 1
2021-09-18	5938 ± 177	3 ± 1
2021-09-19	5792 ± 213	3 ± 1
2021-10-05	5868 ± 299	4 ± 3
2021-10-12	5792 ± 272	4 ± 2
2021-10-19	5772 ± 424	3 ± 3
2021-10-22	5832 ± 348	4 ± 3
2021-10-26	5746 ± 221	3 ± 1
2021-11-15	5898 ± 173	3 ± 1
2021-11-21	5878 ± 365	3 ± 3
2021-12-08	5853 ± 247	4 ± 2
2021-12-20	5777 ± 211	3 ± 1
2022-01-03	5640 ± 241	3 ± 2
2022-02-08	5827 ± 252	3 ± 1
2022-02-17	5853 ± 208	3 ± 1
Mean	5826 ± 262	3 ± 2

This paper has been typeset from a $\text{\TeX}/\text{\LaTeX}$ file prepared by the author.